NAVAL POSTGRADUATE SCHOOL

MONTEREY, CALIFORNIA

THESIS

EFFECTS OF MIXED LAYER SHEAR ON VERTICAL HEAT FLUX

by

Stephen M. Fleet

December 2016

Thesis Advisor:	Tim Stanton
Second Reader:	Timour Radko

Approved for public release. Distribution is unlimited.

Reissued 21 Feb 2017 with correction to spelling of Second Reader's name.

THIS PAGE INTENTIONALLY LEFT BLANK

REPORT DOCUMENTATION PAGE	*Form Approved OMB No. 0704–0188*

1. AGENCY USE ONLY *(Leave blank)*	2. REPORT DATE December 2016	3. REPORT TYPE AND DATES COVERED Master's thesis	
4. TITLE AND SUBTITLE EFFECTS OF MIXED LAYER SHEAR ON VERTICAL HEAT FLUX		**5. FUNDING NUMBERS**	
6. AUTHOR(S) Stephen M. Fleet			

7. PERFORMING ORGANIZATION NAME(S) AND ADDRESS(ES)
    Naval Postgraduate School
    Monterey, CA 93943-5000
		8. PERFORMING ORGANIZATION REPORT NUMBER	

9. SPONSORING /MONITORING AGENCY NAME(S) AND ADDRESS(ES) N/A		**10. SPONSORING / MONITORING AGENCY REPORT NUMBER**	

11. SUPPLEMENTARY NOTES The views expressed in this thesis are those of the author and do not reflect the official policy or position of the Department of Defense or the U.S. Government. IRB Protocol number ____N/A____.

12a. DISTRIBUTION / AVAILABILITY STATEMENT Approved for public release. Distribution is unlimited.	12b. DISTRIBUTION CODE

13. ABSTRACT (maximum 200 words)

   Measurements of salinity, temperature, and velocity shear profile time series were calculated from collocated AOFB and ITP buoys deployed in the Beaufort Sea from 2014–2015. Of interest was the effect ice speed has on MLD shear generation, Richardson number, and heat flux. The inertial components were also considered, as a large inertial event was present during the beginning of the data set. Data from the buoys show turbulent activity in the ocean during inertial wind events contributes to enhanced mixing in the mixed layer and entrainment of heat from the pycnocline. Data during non-inertial events has a much weaker correlation. Results demonstrated that during inertial events, ice speed was moderately correlated with heat flux ($r = .56$, $p < .001$). Non-inertial events saw a lower correlation of ice speed to heat flux ($r = .312$, $p < .001$). Relationships between ice speed and shear ($r = .107$, $p < .001$), ice speed and inverse Richardson number ($r = .035$, $p = .256$), inverse Richardson number and heat flux ($r = .3$, $p < .001$), heat content and heat flux ($r = .084$, $p < .001$) were also explored.

14. SUBJECT TERMS inertial oscillations, inertial motion, arctic, heat flux, entrainment, Richardson number, ice-tethered profiler, autonomous ocean flux buoy, acoustic Doppler current profiler.	15. NUMBER OF PAGES 75
	16. PRICE CODE

17. SECURITY CLASSIFICATION OF REPORT Unclassified	18. SECURITY CLASSIFICATION OF THIS PAGE Unclassified	19. SECURITY CLASSIFICATION OF ABSTRACT Unclassified	20. LIMITATION OF ABSTRACT UU

THIS PAGE INTENTIONALLY LEFT BLANK

EFFECTS OF MIXED LAYER SHEAR ON VERTICAL HEAT FLUX

Stephen M. Fleet
Lieutenant Commander, United States Navy
B.S., Virginia Tech, 2007

Submitted in partial fulfillment of the
requirements for the degree of

**MASTER OF SCIENCE IN METEOROLOGY AND PHYSICAL
OCEANOGRAPHY**

from the

**NAVAL POSTGRADUATE SCHOOL
December 2016**

Approved by: Tim Stanton
                      Thesis Advisor

                      Timour Radko
                      Second Reader

                      Peter Chu
                      Chair, Department of Oceanography

THIS PAGE INTENTIONALLY LEFT BLANK

ABSTRACT

Measurements of salinity, temperature, and velocity shear profile time series were calculated from collocated AOFB and ITP buoys deployed in the Beaufort Sea from 2014–2015. Of interest was the effect ice speed has on MLD shear generation, Richardson number, and heat flux. The inertial components were also considered, as a large inertial event was present during the beginning of the data set. Data from the buoys show turbulent activity in the ocean during inertial wind events contributes to enhanced mixing in the mixed layer and entrainment of heat from the pycnocline. Data during non-inertial events has a much weaker correlation. Results demonstrated that during inertial events, ice speed was moderately correlated with heat flux ($r = .56, p < .001$). Non-inertial events saw a lower correlation of ice speed to heat flux ($r = .312, p < .001$). Relationships between ice speed and shear ($r = .107, p < .001$), ice speed and inverse Richardson number ($r = .035, p = .256$), inverse Richardson number and heat flux ($r = .3, p < .001$), heat content and heat flux ($r = .084, p < .001$) were also explored.

THIS PAGE INTENTIONALLY LEFT BLANK

TABLE OF CONTENTS

THIS PAGE INTENTIONALLY LEFT BLANK

LIST OF FIGURES

LIST OF ACRONYMS AND ABBREVIATIONS

ADCP	Acoustic Doppler Current Profiler
AIDJEX	Arctic Ice Dynamics Joint Experiment
AOFB	Autonomous Ocean Flux Buoy
IOBL	Ice Ocean Boundary Layer
ITP	Ice Tethered Profiler
MLD	Mixed Layer Depth
PSD	Power Spectral Density
SHEBA	Surface Heat Budget of the Arctic Experiment

THIS PAGE INTENTIONALLY LEFT BLANK

ACKNOWLEDGMENTS

THIS PAGE INTENTIONALLY LEFT BLANK

I. INTRODUCTION

A. ARCTIC ENVIRONMENT

The Arctic environment is of great interest to modern researchers in studying global climate change. The sensitivity to summer solar heating, along with limited human contact, offers a prime environment for research. However, there are no illusions about the grueling nature of the Arctic environment. Frigid temperatures and remoteness do not come easy on humans and equipment. Importantly, the under-ice ocean structure and mixed layer dynamics are substantially different than most lower latitude environments. Research in this field is ongoing, with much of it directed at improving coupled atmosphere–ice–ocean numerical models that are gaining predictive skill in this complex region. It is of hope that this research will contribute to that understanding.

1. Air-Ice-Ocean Coupling

The Arctic environment is different than lower latitude oceans because of the presence of the ice pack for most of the year and the strong density stratification that separates the mixed layer from the rest of the underlying ocean. This stratification is unique in that it effectively insulates the surface ice from warmer water that would otherwise create a rapid ice retreat in extent and thickness. The ice pack dampens momentum and energy transfer between the atmosphere and underlying ocean. Previous observations have shown that the Arctic internal wave field is one to two orders of magnitude less energetic than regions in the midlatitudes (Halle and Pinkel 2003; Levine et al. 1985). The low thermal conductivity of the Arctic ice pack also limits sensible heat fluxes between the atmosphere and ocean, while the high albedo and opacity of the ice cover limits transmission of summer-time solar radiation into the ocean. As ice velocity increases in response to wind speed, part of the atmospheric surface stress is transferred into internal ice stresses and deformation, particularly during winter months when the ice concentration is at its greatest (Smith and Grebmeier 1995; McPhee 2008). As the ice pack accelerates, movement of the ice relative to the ocean causes the formation of a sheared Ice-Ocean Boundary Layer (IOBL). With greater under-ice basal roughness, greater momentum

transfer and turbulence generation occur. However, the basal ice surface can often be nearly hydraulically smooth, particularly with new, first year ice, reducing momentum transfer into the underlying ocean for a given ice speed. During summer months, the ice thins, breaks apart, and begins to retreat. Figure 1 demonstrates this breakup of ice.

Winter pack ice   Melt season   Summer ice cover or MIZ
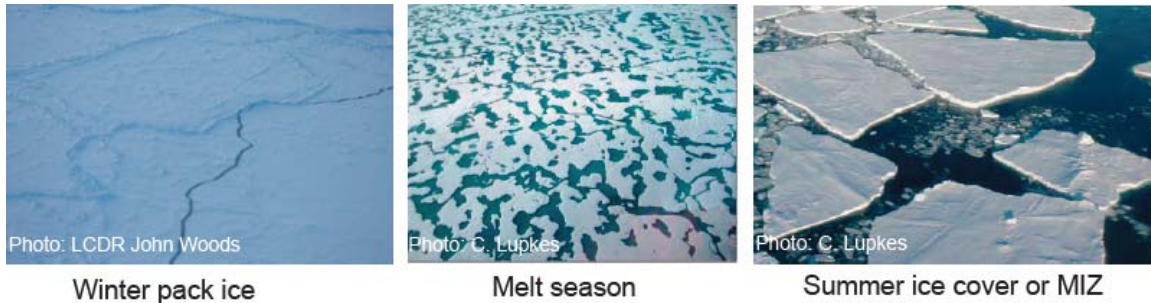
Arctic ice covering during different parts of the year. Note the melt ponds occurring during the melt season, and the breakup of ice during the summer season. The breakup of ice can also occur near Marginal Ice Zones (MIZ), where open ocean meets the Arctic ice pack.

Figure 1. Aerial View of Arctic Seasons. Source: Tsamados et al. (n.d.).

This opening of the ice allows more direct momentum transfer into the ocean from the atmosphere. Consequently, this process acts as a positive feedback mechanism whereby greater surface turbulence enhances ice breakup and mixing, further allowing wind events to penetrate to the ocean surface.

2.   Mixed Layer and Pycnocline Entrainment

The region below the IOBL to the first vertical density gradient (or pycnocline) is called the mixed layer. Attributes of the mixed layer involve nearly uniform temperature and salinity profiles, largely driven by turbulent mixing and forced by motion of the ice relative to a mostly stationary ocean, and in freezing conditions, a buoyancy flux from dense brine being rejected from the forming ice. The ocean mixed layer can be considered an *ice bath* since it is always near the freezing temperature of seawater. In polar regions, the temperature and salinity range of seawater is such that density is controlled by salinity and not temperature. At temperatures close to freezing, the thermal expansion factor B_T of seawater is greatly diminished compared to the haline contraction

factor, B_S. Thus, the impact of B_S is greater in the mixed layer and density becomes a product of the salinity with no attribution to temperature (Figure 2).

β Ratios Versus Temperature (S=34)

$\beta_T/\beta_T(T_f)$

$\beta_S/\beta_S(T_f)$
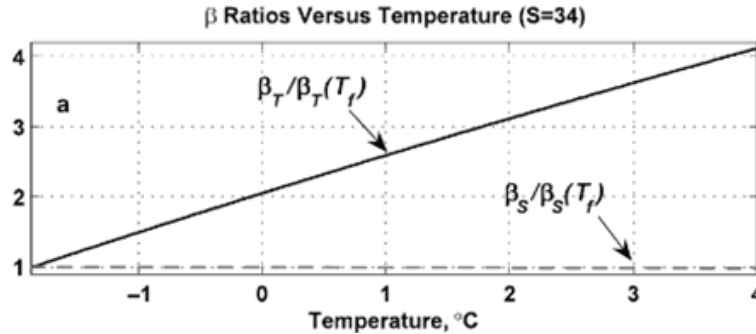
Temperature, °C

Thermal expansion factor ratio increases over 400% from the seawater freezing temperature of -1.86°C to 4°C. Haline contraction factor ratio varies less than 2% throughout the temperature range and is otherwise not sensitive to temperature. Near freezing, the effect of B_T is diminished.

Figure 2.   Thermal Expansion and Haline Contraction. Source: McPhee (2008).

In summer conditions in the Central Arctic the sun is up continuously, delivering substantial radiative fluxes to the ice and ocean surface. Solar radiation penetrates leads (gaps between ice floes). In late summer, the rate of upward heat flux from the ocean will begin to exceed the rate at which conduction can remove the heat to the atmosphere. Downward heat flux from the atmosphere also begins to melt the ice and snow surface when the ice temperature increases towards zero. An example of this is was observed during the Arctic summer of 2007, where Perovich et al. (2008) records a 2.1 m loss of ice thickness due to bottom melting, and a .6 m loss due to surface melting. Solar radiation also drives the formation of melt ponds, which changes the albedo from the 0.85 range of ice and snow to 0.15 range of water. Consequently, the large meltpond areas seen in late summer capture large amounts solar heat and act as a positive feedback mechanism in summertime melt (Gallaher et al. 2016).

Ice melt results in freshwater discharge into the mixed layer, reducing its salinity and frequently creating a shallow pycnocline in light to moderate wind forcing conditions (McPhee 2008, Gallaher et al. 2016). Figures 3 and 4 demonstrate the effect of buoyancy flux.
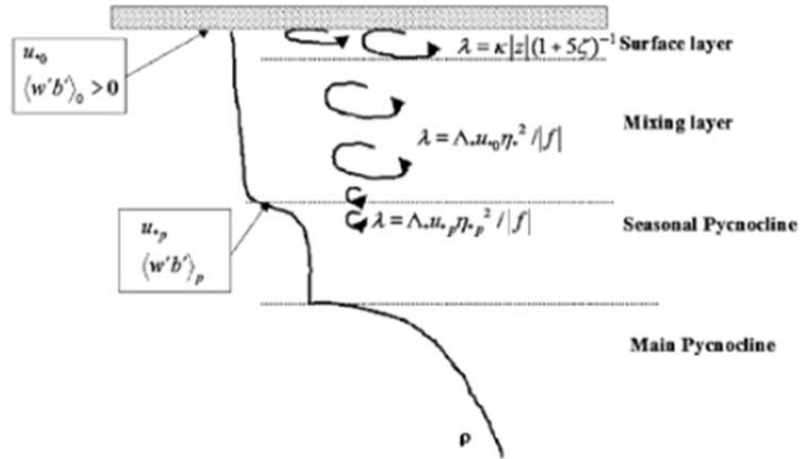
Summer time scenario. Ice melt creates positive buoyancy flux, enhancing stability and often creating a seasonal pycnocline.

Figure 3. Summer time Arctic Vertical Density Profile. Source: McPhee (2008).

During the extreme atmospheric cold of Arctic winters, open water rapidly freezes, reducing the open water fraction as the ice pack thickens. As seawater freezes into ice, brine rejection takes place, increasing the salinity of the mixed layer.
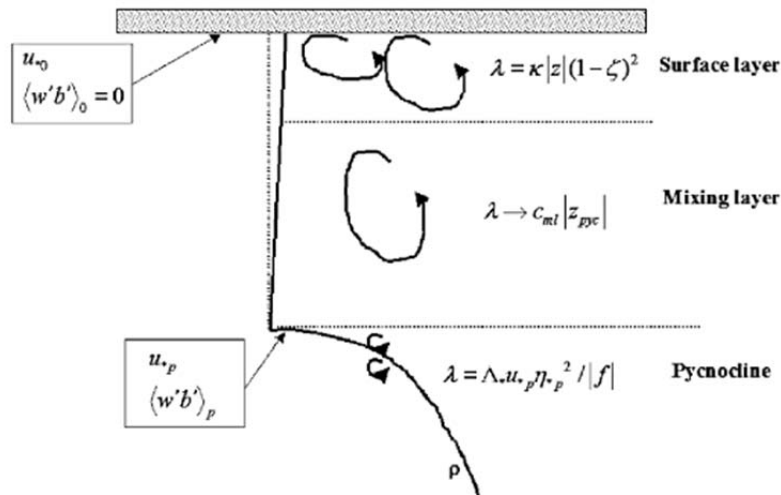
Winter time scenario. Freezing creates a destabilization and negative buoyancy flux due to brine discharge.

Figure 4. Winter time Arctic Vertical Density Profile. Source: McPhee (2008).

Although counterintuitive, brine discharge actually weakens the pycnocline stratification, as changes in density with depth are reduced (Serreze and Barry 2005). The negative buoyancy flux associated with brine discharge enhances turbulence levels in the mixed layer and subsequently mixes down to the pycnocline.

In either the summer or winter scenarios, the main pycnocline plays a critical role in insulating the ice from sub-pycnocline sensible heat (Aagaard et al. 1981). Pacific or Atlantic origin water resides beneath the pycnocline and contains heat capable of melting ice (Figure 5). Although warmer than the freezing temperatures of the mixed layer, the Pacific and Atlantic origin water are much saltier than the relatively fresh mixed layer, giving them greater density, which isolates the fluid from turbulent mixing.
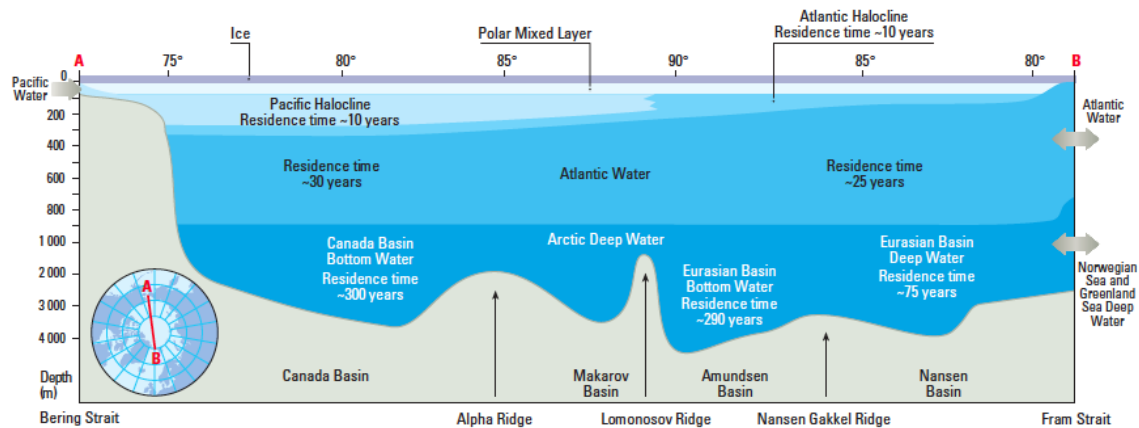
Generalized Arctic vertical cross-section from the Bering Strait to Fram Strait delineating spatial differences in the Arctic water and nomenclature.

Figure 5. Arctic Cross-Section from Bering Strait to Fram Strait. Source: Arctic
Monitoring and Assessment Program (AMAP) (1998).

Turbulence in the ocean mixed layer arising from the wind-driven ice motion is blocked or rapidly diminished through the strong stratification of the pycnocline. The result of turbulent eddies acting on the pycnocline are a sharpening of the density gradient at the base of the mixed layer, a deepening of the pycnocline, and entrainment of heat and salt from the pycnocline. Vertical shear from turbulent surface boundary layer begins to erode the pycnocline which reduces the salinity difference between the mixed

layer and the sub-pycnocline waters, but sharpens the gradient between them (Smith and Grebmeier 1995). Upward heat flux takes place with entrainment, however, the mixed layer remains near freezing due to latent heat of fusion from the melting ice. The net result of a strong pycnocline is an attempted decoupling of the mixed layer from the underlying sensible heat. In the absence of this strong stratification, surface-forced turbulent entrainment would be much greater than what is currently observed in the Arctic.

3.   Inertial Motion

Near-Inertial internal waves have near zero vertical displacement and a horizontal path following a circular, anticyclonic orbit. Gill (1982) describes inertial motion as being synonymous with a *Poincare* wave oscillating at the Coriolis frequency. Since the restoring force of gravity is very weak, the wave takes a path that is similar to a particle moving in the absence of forces; hence the link to *inertia* (Pond and Pickard 1978).

Inertial motion of the ice cover is frequently generated via strong, fast-moving wind events that essentially impose an impulse of momentum on the ice cover. Synoptic-scale weather systems impart wind stress on the ice, which allows momentum transfer to the underlying mixed layer. The ice and mixed layer accelerate, and begin to turn anti-cyclonically due to Coriolis (Figure 6). When the wind ceases, the inertial motion continues, creating a resonant and oscillatory response that can last several days past the actual wind event (D'Asaro et al. 1995; McPhee 2008; Gill 1982; Pond and Pickard 1978).
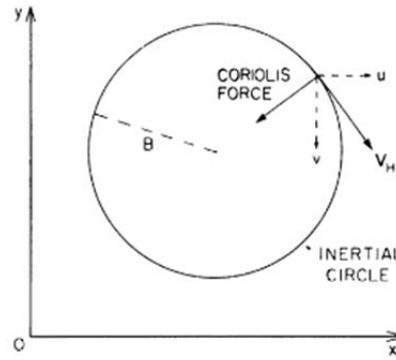
Idealized inertial circle with radius *B*. *u* and *v* are component velocities and V_H is overall velocity. Inertial motion displacement is almost entirely horizontal, making gravity as a restoring force extremely weak. As such, the Coriolis force acts as the restoring force.

Figure 6. Inertial Motion. Source: Pond and Pickard (1978).

As the inertial motion of ice continues, it accelerates the ocean mixed layer, creating shear and turbulence in the mixed layer until most of the shear is concentrated across the density jump at the base of the mixed layer. This mixing and shear contributes to heat and salt entrainment (D'Asaro 1995). It is important to note that not all strong wind events will create strong inertial motion. As Halle and Pinkel (2003), and D'Asaro (1985) demonstrated, inertial events can be hampered by mesoscale eddies and sub-inertial motion. These hindrances can act as a dampening mechanism on not only the strength of the inertial motion, but also on the depth of which the inertial motion penetrates. The spatial and temporal scale of the wind events strongly effect the strength of the inertial response. McPhee (2008) also notes that internal ice stress can dampen inertial motion through ridge formation.

4.   Declining Ice Thickness and Extent

The decline in ice thickness and extent is not only a telling sign of Arctic warming, but also suggests a positive feedback mechanism. The decadal average for loss of sea ice extent was 3–4% from 1979–2012 with a 43% decrease in thickness (Wadhams 2012; IPCC 2014). After 1996, the loss of sea ice extent increased to 10% per decade (Figure 7). Every successive decade in every season has seen a decrease in Arctic sea ice extent since 1979 (IPCC 2014).

7
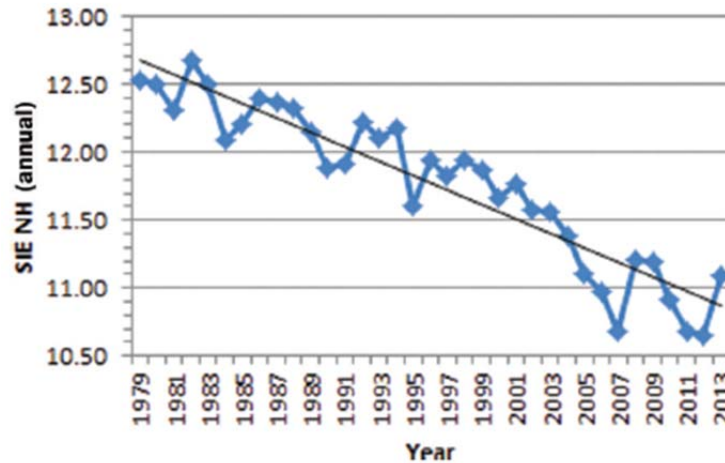
Annual average of Northern Hemisphere sea ice extent (10^3 km^2) from 1979 through 2013. Solid black line represents linear regression.

Figure 7. Historical Sea-Ice Extent. Source: Simmonds (2015).

Declining ice thickness and extent has widespread impacts. A decrease in in ice covering, particularly snow covered multi-year ice, reduces albedo. The increase in solar insolation reaching the water from lack of ice magnifies the warming of the Arctic. With Arctic warming, there is a decrease in multi-year ice relative to first-year ice. First year ice has a largely hydraulically smooth base, and it is thinner and does not insulate from downward heat flux during warmer atmospheric temperatures in the summer months. Thermal coupling between the atmospheric boundary layer and underlying seawater increases (Wadhams 2012; McPhee 2008; Randall et al. 1998). Although this is ameliorated via more rapid formation of first year ice and subsequently less turbulent exchange from under-ice roughness, first year ice does not typically survive annual or biennial summer seasons without significant snow covering (Maykut 1978). In general, with an overall increase in heat reaching the ice-ocean-boundary layer, the result is still increased ice melt. Larger open water area allows for greater wind fetch, which contributes to greater surface wave energy and subsequent ice breakup in the marginal ice zone.

With the Arctic warming also comes greater risks from seawater steric expansion, increased export of fresh water to the Northern Atlantic, ocean conveyor belt inhibition, permafrost melting, ecological and economic damage, and stronger storms. Although the

8

warming is in the Arctic, it is coupled with the rest of the planet. Oceanic currents, atmospheric patterns, and particular flora and fauna are significantly impacted.

B.   BACKGROUND

Toole et al. (2010) studied the influences of the thermohaline stratification in the central Canadian basin and its effects on basal melt rate of sea ice. In a large study utilizing over 6500 individual temperature and salinity profiles from the Woods Hole Oceanographic Institute between summer 2004 and summer 2009, Toole et al. (2010) created a 1-D ocean mixed layer model to calculate heat flux estimates in the Canadian Basin. The profiles were measured by 10 Ice Tethered Profilers, which entered the Canadian Basin during their lifespan. Results demonstrated an average summertime mixed layer depth of 16 m, with average wintertime mixed layer depth of 24 m. Toole et al. (2010) noted limitations of the ITP in measuring right up to the ice. These limitations occurred in later summertime with the presence of a seasonal pycnocline that was very near to the 9 m minimum sample depth of the ITP. These shallow density jumps in controlling turbulent mixing in the ocean mixed layer.

Toole et al. (2010) compared these temperature and salinity profiles to 1975 profiles taken during the Arctic Ice Dynamics Joint Experiment (AIDJEX). Results had shown that the winter mixed layer in 1975 had a weaker density stratification and greater depth. Summertime mixed layer salinity in 1975 had less contrast with the wintertime, and lacked a near surface temperature maximum due to solar insolation. The Canadian Basin had become warmer and fresher compared to 1975. The summertime 1-D model used had good agreement with the observations, and estimated that out of the 65 W m^{-2} of incoming shortwave radiation, 50 W m^{-2} went to bottom melt, with 15 W m^{-2} going to increasing ocean heat content. Toole et al. (2010) noted that the 15 W m^{-2} would appear as a temperature increase in the near surface temperature maximum. The wintertime 1-D model used a 15 W m^{-2} cooling rate, which averaged to a 70 cm ice growth over the study period. The 1-D model allowed the calculation of turbulent diapycnal diffusivity, which is the heat from turbulent mixing that is required to match the authors' heat budget. The turbulent diapycnal diffusivity was estimated to be several orders of magnitude larger

than cited in previous literature. This led to the conclusion that pycnocline stratification is currently isolating the sea ice from deeper sensible heat in the Canadian Basin, primarily from Pacific Summer Water (PSW) that lies between 40—100 m depth. During the 1-D model runs, Toole et al. (2010) applied over 3 times the cooling rate and an order of magnitude larger mechanical work, still the PSW water failed to significantly entrain. They did find that near surface temperature maximums created during the summertime can be entrained into the mixed layer and contribute to delayed fall ice growth. An interesting negative feedback mechanism was that increased basal mixed layer stratification since 1975 would require increased turbulent energy to entrain sub-mixed layer sensible heat. However, decreased thickness of the mixed layer would also concentrate the turbulence, allowing for greater entrainment—hence the counteracting physical mechanisms.

Toole et al. (2010) defined the mixed layer by finding the first instance in potential density that exceeded a reference potential density by .01 kg m^{-3}. The reference potential density was the shallowest sampled potential density in each profile. Timmermans et al. (2012) used a similar method but also defined a layer beneath the mixing layer termed the surface layer, with a potential density difference of .25 kg m^{-3} from the reference potential density. Timmermans et al. (2012) found that lateral processes from ageostrophic baroclinic instability can restratify the surface layer after a mixing event. This restratification can effectively block vertical shear and dynamical processes. Between the mixing layer (.01 kg m^{-3}) and surface layer (.25 kg m^{-3}), Timmermans et al. (2012) defined this gap as the insulating layer. The insulating layer, combined with the restratification of the mixed layer from baroclinic instability, shields the underlying basal surface layer from erosion and entrainment of heat and salt. This interesting aspect of restratification acts as a negative feedback mechanism to mixing and further isolates the warm PSW.

Shaw and Stanton (2014) studied the upper ocean vertical temperature diffusivity in the western Arctic ocean using data sets collected from the one year duration 1997–1998 Surface Heat Budget of the Arctic Experiment (SHEBA) manned ice camp. Data collected from a winch operated profiler with thermal microstructure package recorded

CTD data to a depth of 160 m. Of the 12,350 casts made, 9395 had adequate quality CTD and thermal microstructure data. The SHEBA ice camp and subsequently the profiling equipment drifted over multiple bathymetric features such as the Canada Basin, Chukchi Borderlands, and Mendeleev Abyssal Plain. Shaw and Stanton (2014) calculated vertical turbulent temperature diffusivities based upon the Osborn and Cox (1972) model in which the production and dissipation of turbulent potential temperature variance is assumed to be in statistical balance. Results varied spatially according to the underlying bathymetric features of the ice camp. For the Canada Basin, heat flux was an average of .1 W m^{-2} into the mixed layer. The Chukchi Borderlands saw an average heat flux of 2 W m^{-2} into the mixed layer and the Mendeleev Abyssal Plain saw a near zero vertical heat flux. Vertical diffusivity values away from irregular bathymetry were on the order of 10^{-7} m^2 s^{-1}; meanwhile, vertical diffusivity values near ridges and plateaus were on the order of 10^{-6} m^2 s^{-1}. The underlying ridges and plateaus were largely in the Chukchi Borderlands, which consists of the Northwind Ridge, Southern Chukchi Plateau, and Northern Chukchi Plateau. Periods of intense surface forcing saw vertical diffusivity values on the order of 10^{-4} m^2 s^{-1}, although specific instances were not discussed.

Shaw and Stanton (2014) concluded that halocline diffusivities near the Canada Basin are very near molecular diffusion levels Although vertical diffusivity is an order of magnitude larger near bathymetric features in the Chukchi Borderlands, the level is still quite small when compared to historical diffusivities near the Yermak Plateau and Lomonosov Ridge. The Chukchi Borderlands enhanced heat flux is correlated with an increase in the vertical strain variance. This provides a connection between inertial wave activity, turbulence, and bathymetric features. Shaw and Stanton (2014) note that even if vertical temperature diffusivities remain unchanged since SHEBA, the Chukchi Borderlands can still expect increased ice retreat if sensible heat is increased in the subsurface temperature maxima. Given future ice retreat, the vertical diffusivities may change with changes in turbulence and mixing.

Shaw et al. (2009) studied data acquired from the SHEBA experiment again with an emphasis on heat budget and its effects on sea ice. Similar to results found in Shaw and Stanton (2014), when the ice camp north off of the Chukchi shelf, very little

entrainment took place. Although there was a lack of irregular bathymetry, there was also a lack of Pacific halocline water from which to entrain heat. Even with a saltier mixed layer and subsequently reduced stratification, a lack of Pacific origin water attributes to a *cool* halocline, thus the nearest sensible heat is beyond reach deep in the Atlantic halocline. Interestingly, during the summer heating day, particularly record days 575–640 of 1998, incoming solar radiation provided an upward heat flux average of 16.3 W m^{-2}. This dwarfed the flux due to upper pycnocline entrainment (.1–1.5 W m^{-2}). Price et al. (1986) studied extensively the effects of solar insolation and mixed layer dynamics in the eastern Pacific Ocean. Although ice cover is not present, Price et al. (1986) found that solar insolation heats the surface layer and creates a near surface stratification. Higher wind velocities deepen and erode the stratification, increasing the overall temperature of the mixed layer. The difference in the Arctic is that solar insolation heat is immediately available for basal ice melt since it is primarily trapped in the IOBL.

Levine et al. (1985) studied the internal wave energy levels of the Arctic and compared them to observations at lower latitudes. A single thermistor chain with 2 min sampling intervals and 10 m resolution was moored under the ice pack in the vicinity of the Yermak Plateau from 01–06 May 1981. Additionally, the researchers used a profiling current meter and CTD. Fourier transforms with ensemble averaging and non-overlapping frequency bands were used to convert the timeseries data into spectra. The inertial frequency based on deployment latitude was .0825 cph, with a local buoyancy frequency (*N*) between 2—4 cph at MLD depths. Depths of individual isotherms were tracked in time, with the assumption made that vertical displacement is dominated by internal waves. Results demonstrated an internal wave energy spectrum that is less energetic by a factor of 10^1 to 10^2 (Levine et al. 1985; Pinkel 2008). Aagaard (1981) and Halle and Pinkel (2003) found similar results in reduced internal wave energy. Frequency dependence between the inertial and buoyancy frequency was to the power of -1.5 to -2; close but less than the Garrett and Munk (1972) spectral slope.

Levine et al. (1985) argues that the lack of significant internal wave energy is due to ice cover dampening the internal wave field, and weakening wind-forced momentum transfer through the ice in comparison with the open ocean. Halle and Pinkel (2003)

12

study of inertial internal wave energy in the Beaufort Sea noted inertial events were not always correlated to ice motion. Indeed, beyond ice cover mentioned in Levine et al. (1985), internal waves near the inertial frequency could be dampened by mesoscale currents, leading to destructive interference of the inertial waves. This interaction also limits subsequent vertical shear, and thus heat and salt flux. They also note that during wind events, greater inertial internal wave energy was found during late winter compared to early winter. This contradiction is noted by the researchers, and is opposite to McPhee (2008) and Levine et al. (1985) findings. Halle and Pinkel (2003) conjecture is that as winter progresses, ice deformation through convergence and divergences creates ridges and leads due to internal stresses. This deformation appears to increase the generation of inertial waves.

C. OBJECTIVES

The purpose of this research was to contribute to the parameterization of geophysical features that are used in coupled ice-ocean-atmosphere numerical models. Many dynamical mechanisms in the Arctic are not well understood, and with a changing Arctic, these features are important to understand if Arctic numerical predictions are to be accurate. The incorporation of more research and in-situ observations will result in decreased model error and extend prediction capabilities.

Of interest in this thesis was the effect of mixed layer dynamics on vertical heat flux. Hypothesis testing occurred between multiple variables, specifically: ice speed and heat flux, ice speed and shear, ice speed and inverse Richardson number, inverse Richardson number and heat flux, and heat content one meter below the MLD against heat flux. The null hypothesis is that no relationship exists between any two variables tested. Type I error less than .05 would reject the null hypothesis.

THIS PAGE INTENTIONALLY LEFT BLANK

II. METHODS

A. EQUIPMENT AND DATA SOURCES

Unattended arctic environment instrumentation must be able to withstand frigid temperatures, lack of routine maintenance, and damage from either polar bears or ice ridging and melting. This presents a challenge when creating autonomous sensors that can run on batteries and transmit data via satellites. Often these unique challenges are overcome through custom building of equipment. This thesis used Ice-Tethered Profilers (ITP) developed by the Woods Hole Oceanographic Institute and an Autonomous Ocean Flux Buoy (AOFB) designed by Tim Stanton at the Naval Postgraduate School (NPS).

1. Ice-Tethered Profilers

The ITP is an automated, moderately priced, expendable, CTD profiling system designed to be deployed on perennial sea ice in the Arctic Ocean (Figure 8). It was developed to provide 1 m resolution temperature and salinity profiles down to a depth of 750 m with a 3-year endurance life cycle (Krishfield et al. 2008). The ITP was built light enough to be transported on Twin Otter aircraft or helicopters and slim enough to be deployed through a 25 cm auger or ice-melt hole.
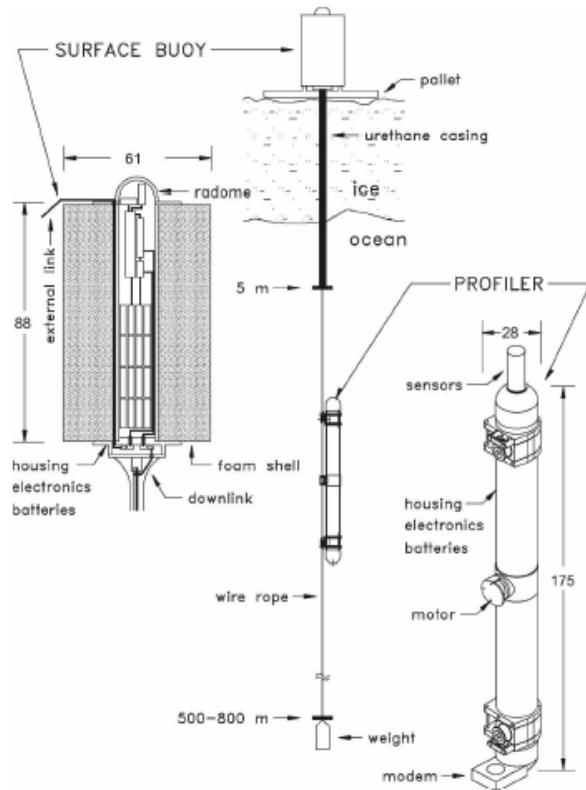
Figure 8. ITP schematic. Source: Krishfield et al. (2008).

The ITP consists of three components: a surface instrument package, an insulated wire-rope tether, and an underwater profiler. The surface instrument package is a cylindrical housing that sits on top of the ice with a foam shell surrounding the electronics. Within the electronics package is a GPS receiver, data controller, lithium batteries, Iridium 9522 L-band transceiver, and a low-power Persistor CF2 computer. Onboard flashcard memory can store all sensor and engineering data for the life of the system. Data is also passed via the Iridium modem to a dedicated computer at the Woods Hole Oceanographic Institute. The wire-rope tether is a .635 cm insulated steel wire with a 114 kg ballast weight fixed to the bottom. Length of the tethers are often built to reach 750 m in depth, but can be built shorter to accommodate shallower bathymetry at deployment locations. The profiler is a cylindrical case housing batteries, tether-climbing drive system, CTD, and buoyancy controls. The CTD samples at 1 Hz usually while going down the tether. ITP profilers are ballasted to be neutrally buoyant near the middle of the tether depth (Krishfield et al. 2008). The ITP drive system that powers the

movement of the profiler uses approximately 1 W per profile, owing to approximately 1.5 million meters of profiling, or 2.5–3-year lifespan when profiling twice per day. For this deployment, CTD profiles were sampled every 3 hours. Data is made publicly available at Woods Hole Oceanographic Institute's website (www.whoi.edu).

2. Autonomous Ocean Flux Buoys

The AOFB is comprised of two main components: a surface buoy and an instrument package deployed at 4.5m depth (Figure 9). The surface buoy contains a two-way Iridium transceiver, GPS, meteorological package, lithium batteries, solar recharging panels, and onboard processors and computers. Data is uploaded twice-daily to a dedicated computer at NPS (AOFB 2016).
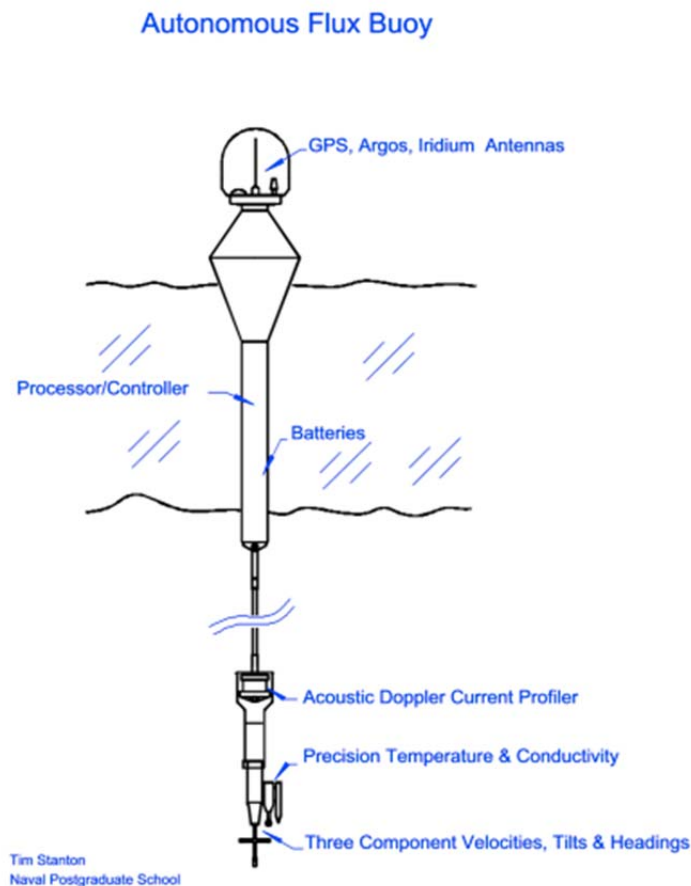

Figure 9. Autonomous Ocean Flux Buoy (AOFB). Source: AOFB (2016).

The instrument package has several components. First is a 300 kHz Acoustic Doppler Current Profiler (ADCP) designed and built by Teledyne Instruments. The ADCP senses current velocity every 2 m in the vertical to a range of up to 80 m using broadband signal processing. This allows the vertical gradient of shear to be calculated through vertical differencing of the horizontal velocity components. The ADCP profiles were sampled every 30 minutes. Second, the AOFB contains a custom built flux package that consists of a 3D current meter, conductivity cell, and fast response thermistor (AOFB 2016). The acoustic travel-time velocity sensor has a noise floor of 0.2 mm/s, and the temperature sensor resolves 30 microkelvin temperature fluctuations. These sensors allow for the calculation of heat, salt, and momentum flux through the use of eddy correlation methods. The flux package was run for 40 minutes every 2 hours to robustly estimate the vertical turbulent fluxes. Ice velocity was derived from 10 minute sampled GPS positions of the AOFB surface buoy. The AOFB is dynamic and constantly being updated. Latest buoy designs include a downward hanging MLD spar unit with FP07 fast response thermistors to measure the thermal diffusivity and vertical heat fluxes within the stratified part of the water column. Future designs will also include a variable depth instrument package that adjust to a specified depth within the IOBL (T. Stanton, 2016, personal communication).

B.   DATA PROCESSING

Data processing steps of the AOFB 29 and ITP 80 timeseries are described in the following section. Both instrument systems were collocated on an intact ice floe in the Beaufort Sea and deployed from the Araon Ice Camp in 2014. All data processing took place on MATLAB version 2016a software. Calculations that required the use of ADCP data were limited to yeardays 246.5 of 2014 to 25 of 2015 due to backscatter conditions. Heat flux and heat content calculations were available from yeardays 246.5 of 2014 to 120 of 2015. Vertical profiles of N^2 were available during the entire life of the ITP (yeardays 226 of 2014 to 143 of 2015).

1.   Potential Density Anomaly

The Mixed Layer Depth (MLD) was calculated from ITP profiles of salinity, temperature, and pressure to produce potential density profiles. Similar to the methods of Timmermans et al. (2012), the MLD was defined via the .25 kg m^{-3} criteria (Figure 10). The potential density at -10 m depth was the first bin that was consistently available through all profiles from the ITP data. This -10 m bin acted as the reference bin in calculating bulk density difference. The reference bin was subtracted from each subsequent depth bin until the potential density difference equaled .25 kg m^{-3}. ITP bins have one meter resolutions; as such, bulk density differences were linearly interpolated to allow greater resolution and precision in establishing the MLD.
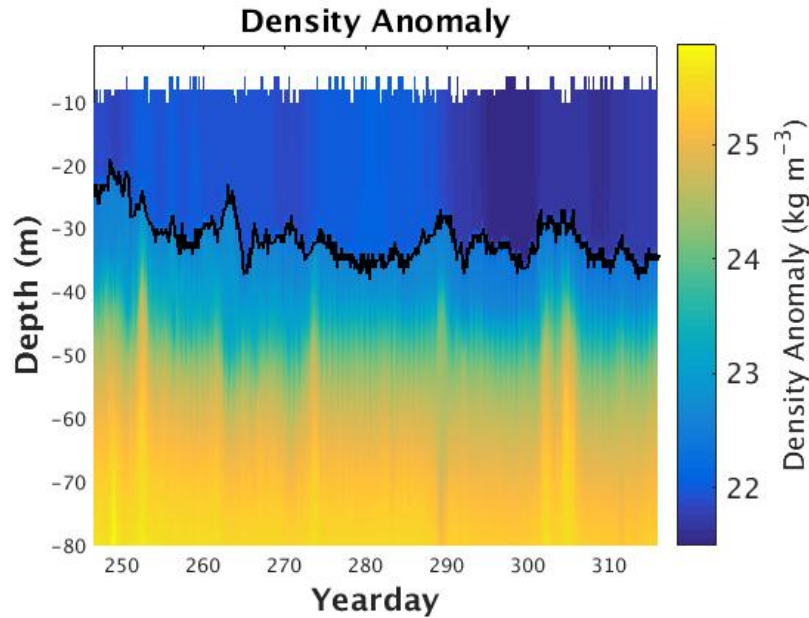
Colored plot of potential density from yeardays 246.5–320 with .25 kg m^{-3} MLD overlaid (black line).

Figure 10. Plot of Potential Density Anomaly and MLD Calculation.

Figure 10 shows a profile timeseries of potential density anomaly calculated from the ITP with the .25 kg m^{-3} MLD overlaid as a black line. As the timeseries progresses towards winter, the MLD is found at greater depths. Variations in the depth of the

observed MLD can be affected by mesoscale eddies, turbulent mixing, and drift of the buoy over regional variability in the upper ocean.

2.   Brunt–Väisälä Frequency

The Brunt–Väisälä frequency, also known as buoyancy frequency, or N, is an angular frequency that represents dynamic stability. It is the oscillation frequency a particle would have if displaced from rest. N^2 is defined as:

$$N^2 = \left(-\frac{g}{\rho} \frac{\partial \rho}{\partial z} \right)$$
,

where g is the gravitational constant (9.8 m s^{-2}), *rho* is the potential density, and z is the depth. Where N^2 is positive, the stratification is stable. Likewise, if N^2 is negative, the stratification is unstable (Gill 1982). N^2 profiles were calculated through depth from the 3hr sampled ITP profiles. Low-pass filtering of N^2 with a 10 hr cutoff was used to limit the effects of high frequency geophysical noise (Figure 11).
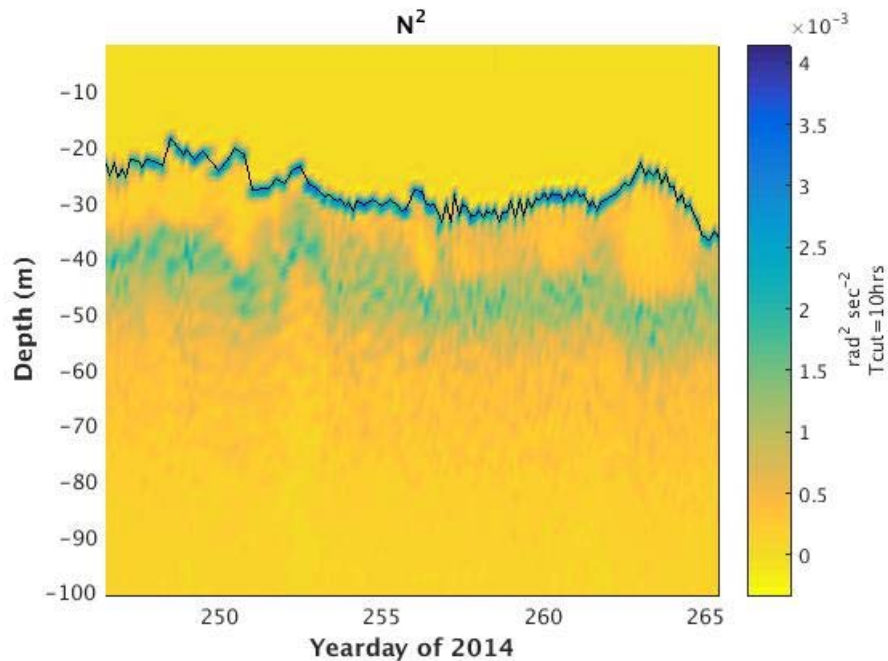
Colored plot of N^2 from yeardays 246.5–266. Black line represents the .25 kg m^{-3} MLD.

Figure 11. Buoyancy Frequency.

With N^2 values and depths determined (Figure 11), vertical linear interpolation was used to find N^2 at MLD depths. Along with N^2, interpolation of shear values to the ITP time frame allows for Richardson number calculations. Just beneath -20 m, the N^2 maximum associated with the upper pycnocline can clearly be seen. The less defined secondary stratification near -40 m represents the Pacific water. Intrusion of the Pacific water through the Bering Strait is incorporated into the Beaufort Gyre and subsequently the Canadian Basin.

3.   ADCP Bad Data Masking

Masking is a technique used to negate data that is likely erroneous due to poor ADCP backscatter and correlation values. Backscatter profiles returned by the ADCP represent the acoustic backscatter strength in each range bin of the profiles. The closer, larger, and greater number of scatterers will give a larger backscatter value. ADCP correlation profiles are an estimate of the correlation levels found in each bin during the broadband Doppler frequency calculation. Correlation values will be high if different echoes from within the same pulse all have the same time lag. An example of high ADCP correlation would be multiple scatterers moving together at the same speed and direction (Gordon 1996). Neither backscatter or correlation are displayed with units due to normalizing within the ADCP (Figure 12).

A running standard deviation in time was used as the ordinate in comparing backscatter and correlation. It is calculated at each individual ADCP sample time by utilizing the data 4 time intervals before, and 4 time intervals after, the current time sample for a total of 9 sample points. This 9-sample point window then slides along through time, calculating standard deviation along the way.
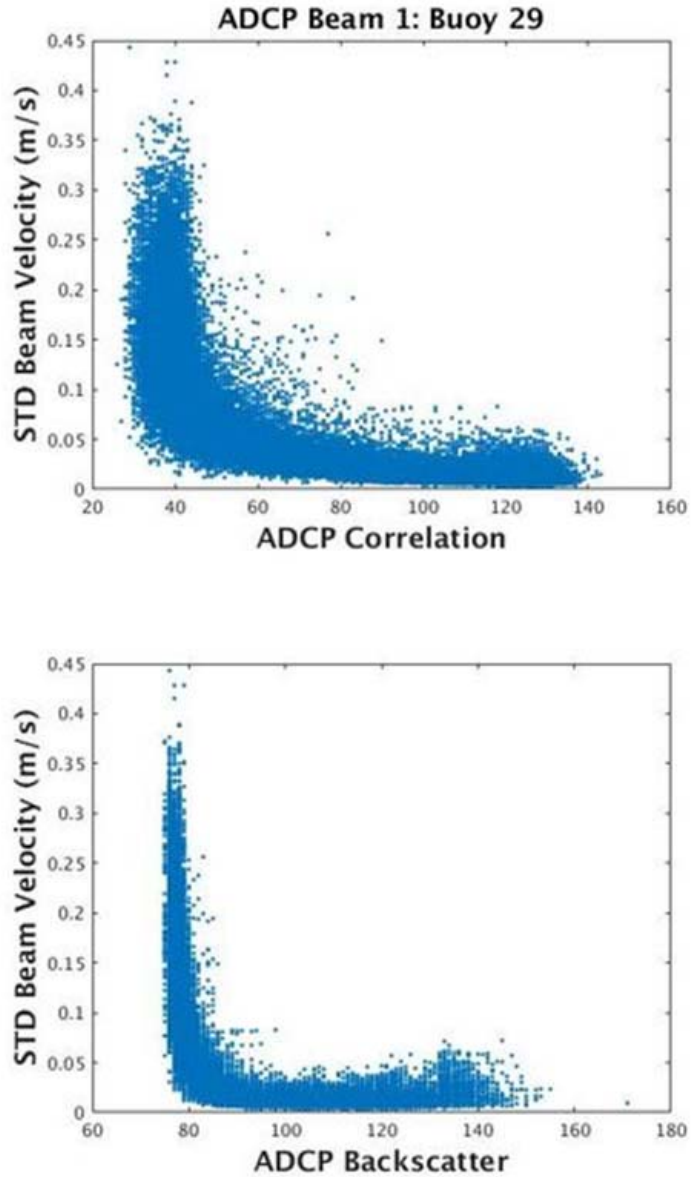
ADCP correlation and backscatter compared to the standard deviation of beam 1 velocity.
Masked data required a backscatter value less than 85 and a correlation less than 45.

Figure 12. ADCP Backscatter and Beam Velocity.

The standard deviation is then compared to the backscatter and correlation values. Noisy velocity data is seen in the rapid rise in standard deviation, for low backscatter or low correlation values (Figure 12). Velocity data with less than a normalized backscatter value of 85 *and* a normalized correlation value less than 45 was turned into *Not a Number* (NaN) in in each profile. Figure 13 shows the process of masking.
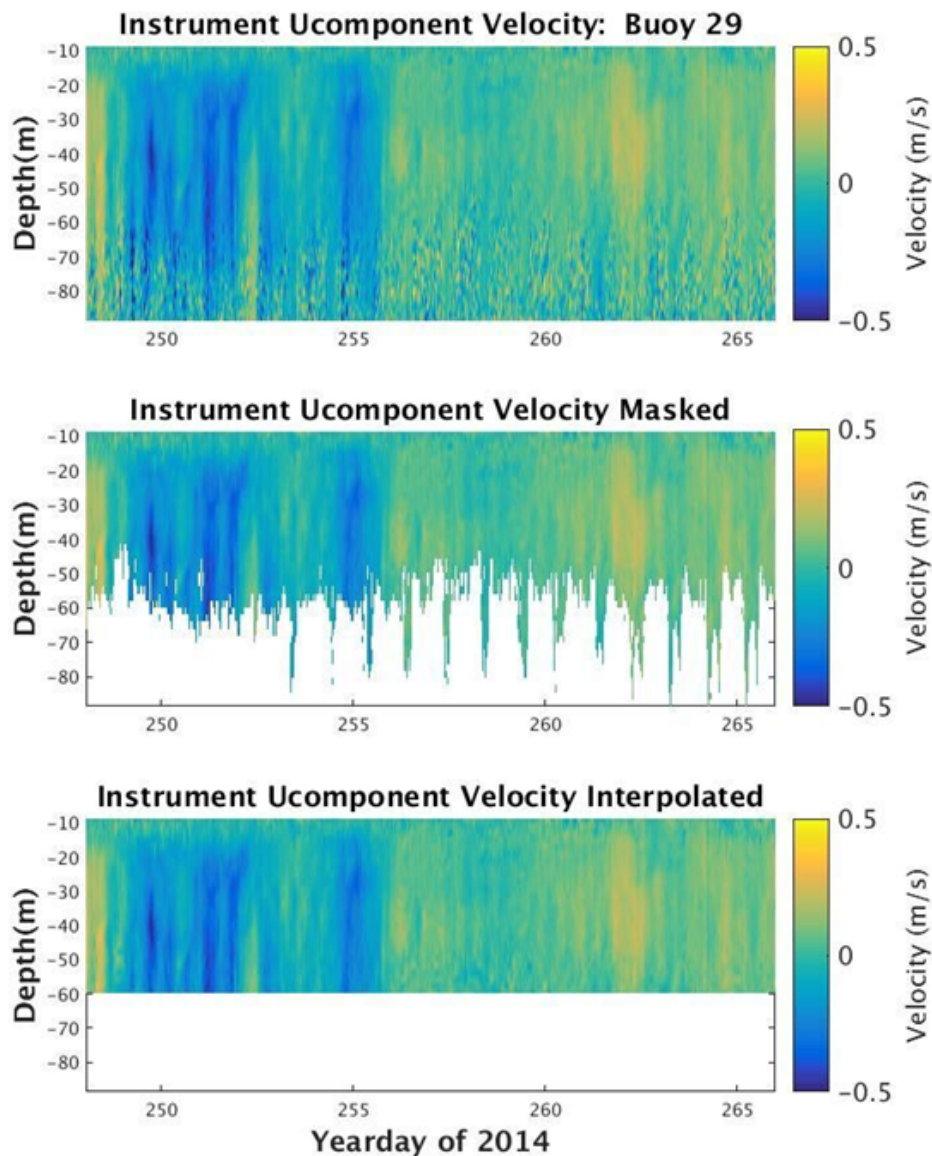
Process of masking for yeardays 246.5–266. Raw ADCP *u* component velocity data (top panel). Masked data with NaNs inserted in erroneous spots (middle panel). Depth bins—59.9 m and less were interpolated through time and kept as usable data (bottom panel).

Figure 13. Masking of Current Velocity.

A decision was made to interpolate through time and keep data at roughly -60 m and shallower. The closest ADCP depth bin to this chosen depth was -59.9 m and was subsequently chosen as the deepest bin used in this analysis. Figure 13, middle panel shows the effect of masking when backscatter and correlation values did not meet the

selected criteria. The bottom panel shows the effect of linearly interpolating the data shallower than -60 m and masking all data that was deeper.
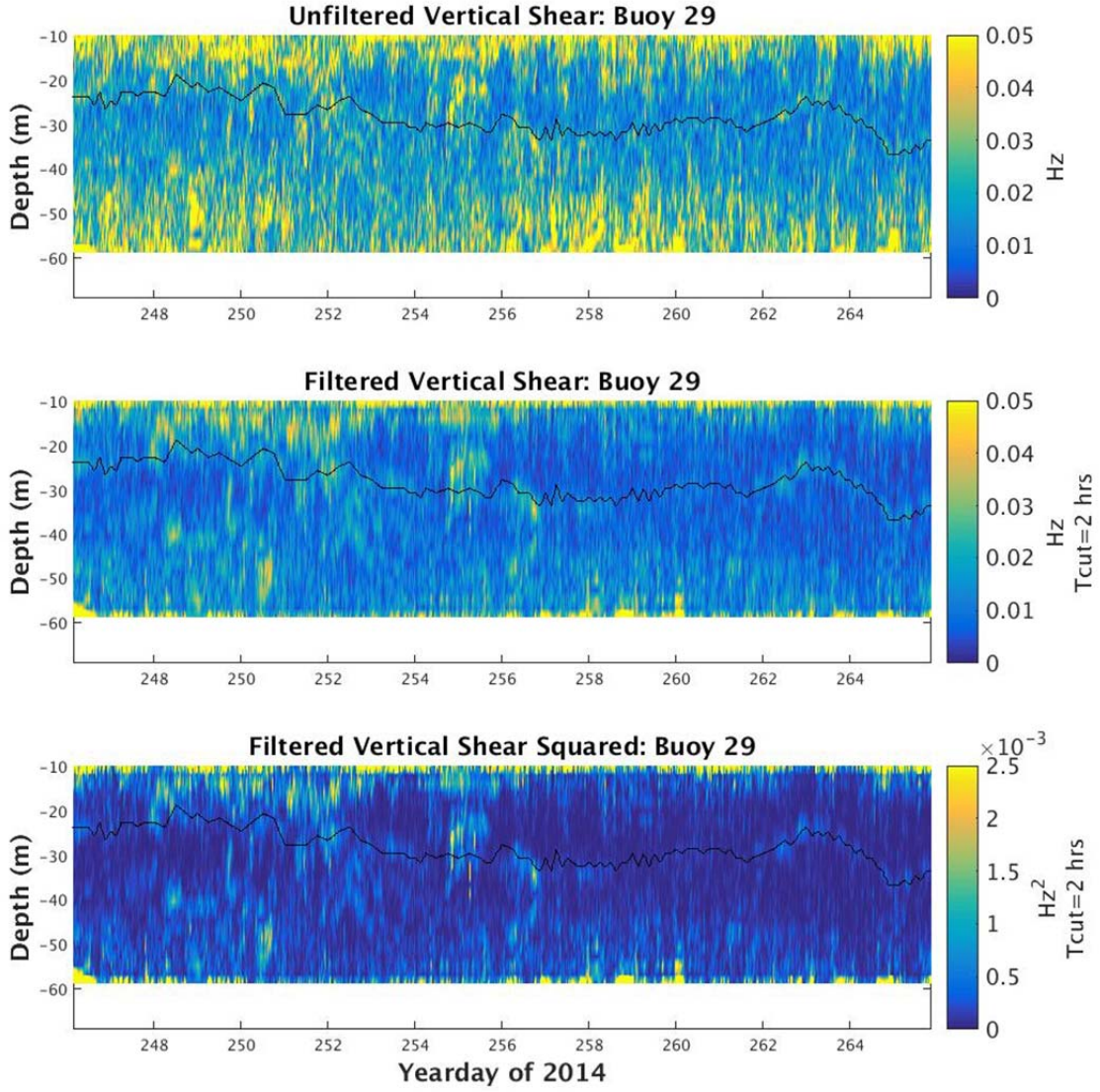
Calculations that involved vertical shear utilized a threshold depth of -58.9 m. Vertical differencing places shear depth bins in-between ADCP depth bins. This process of masking did not interfere with the MLD depth. At no time during the analyzed period did the MLD exceed -58.9 m.

4.   Vertical Shear

ADCP measured current velocities are 30 min averaged, east-west (*u*) and north-south (*v*) components, with depth intervals every 2 m. The first measured depth bin is -8.64 m and ends at -88.64 m. Shear is calculated from these differences in measured velocities with each depth bin. The difference in vector amplitudes of each component are divided by the change in depth (2 m):

$$shear = \sqrt{\left(\frac{\partial \bar{U}}{\partial z}\right)^2 + \left(\frac{\partial \bar{V}}{\partial z}\right)^2}$$

Low pass filtering in time of the 30 min interval samples using a fourth-order Butterworth filter with a period cutoff of 2 hrs was used to limit the impact of high frequency variability. Figure 14 shows the shear profile timeseries as unfiltered, 2 hr filtered, and 2 hr filtered squared shear to show the reduction in both instrument and geophysical noise with filtering. Significant shear noise remained in the upper few bins, but these were not used in the following analyses. The black line in Figure 14 represents the MLD. It is apparent the insulating effect that is taking place between yeardays 248–252 due to the strong stratification. Strong shear is encountered above the MLD during these days, but significantly reduced shear is seen below the MLD. Yeardays 262–266 show shear that closely overlaps with the MLD, again reinforcing the insulating effect of the MLD's strong stratification in preventing turbulent penetration and momentum transfer into the pycnocline.

Vertical shear for yeardays 246.5–266. Unfiltered vertical shear (top panel). Filtered vertical shear (middle panel). Filtered shear squared (bottom panel).

Figure 14. Vertical Shear.

For Richardson number calculations, the squared version of shear is required. In order to evaluate shear across the MLD, a linear weighting function was used on the filtered squared shear profile timeseries:

$$weight = \frac{d_{MLD-1} - d_{MLD}}{d_{MLD-1} - d_{MLD+1}}$$

$$shear^2_{MLD} = s_{MLD-1}(1 - weight) + (s_{MLD+1} \cdot weight)$$

,

where d_{MLD-1} is the depth of the closest ADCP bin that is shallower than the interpolated MLD. Similarly, d_{MLD+1} is the depth of the closest ADCP bin that is deeper than the MLD. d_{MLD} is the actual depth of the MLD. This weighting value is used in the second formula where s_{MLD-1} is the shear squared value in the closest bin that is shallower than the MLD, and s_{MLD+1} is the shear squared in the next deepest bin. $shear^2_{MLD}$ is the derived squared shear at the actual MLD. The square root of $shear^2_{MLD}$ will give us the total shear at the MLD.

5.   Gradient Richardson Number

The dimensionless gradient Richardson number is a measure of whether dynamic turbulence will occur (Pond & Pickard, 1978). Empirically derived, it is the ratio between the shear squared and N^2. A Richardson number less than .25 indicates a high likelihood of turbulence and subsequent heat and salt entrainment.

$$Ri = \frac{N^2}{\left(\frac{\partial \vec{U}}{\partial z}\right)^2 + \left(\frac{\partial \vec{V}}{\partial z}\right)^2}$$

Large values of the Richardson number are often encountered in the ocean, so it is more convenient to use the inverse Richardson number. Inverse Richardson number values greater than 4 would indicate turbulent conditions.

N^2 values are calculated from ITP profiles sampled at a 3 hr sampling interval. Linear interpolation through depth using the MATLAB function *interp1* allowed N^2 values to be obtained at the exact MLD depth for each vertical profile. However, values of *shear* $^2_{MLD}$ were required to be interpolated through time and depth using the MATLAB function *interp2*. *shear* $^2_{MLD}$ values were originally calculated at the ADCP

sample rate of 30 min and at every 2 m depth bins. The MATLAB function *interp2* allows retrieval of *shear* $^2_{MLD}$ at the exact MLD for each 3 hr sampled ITP profile. With both *shear* $^2_{MLD}$ and N^2 at the same time and depth, the inverse Richardson number can be calculated.

6. Determination of Earth Relative Motion

The AOFB contains an accurate Global Positioning System (GPS) with a sample period of 10 min. Earth relative buoy movement was calculated by differences in latitude and longitude, then converted from decimal degrees to meters per second. Local magnetic declination was determined using the MATLAB program *igrfmagm* and applied to the ADCP heading. After the declination correction, regardless of where the AOFB was in the Arctic, the coordinate system had North as toward the true North Pole, and East was always 90° to the right, along a line of latitude (Figure 15).
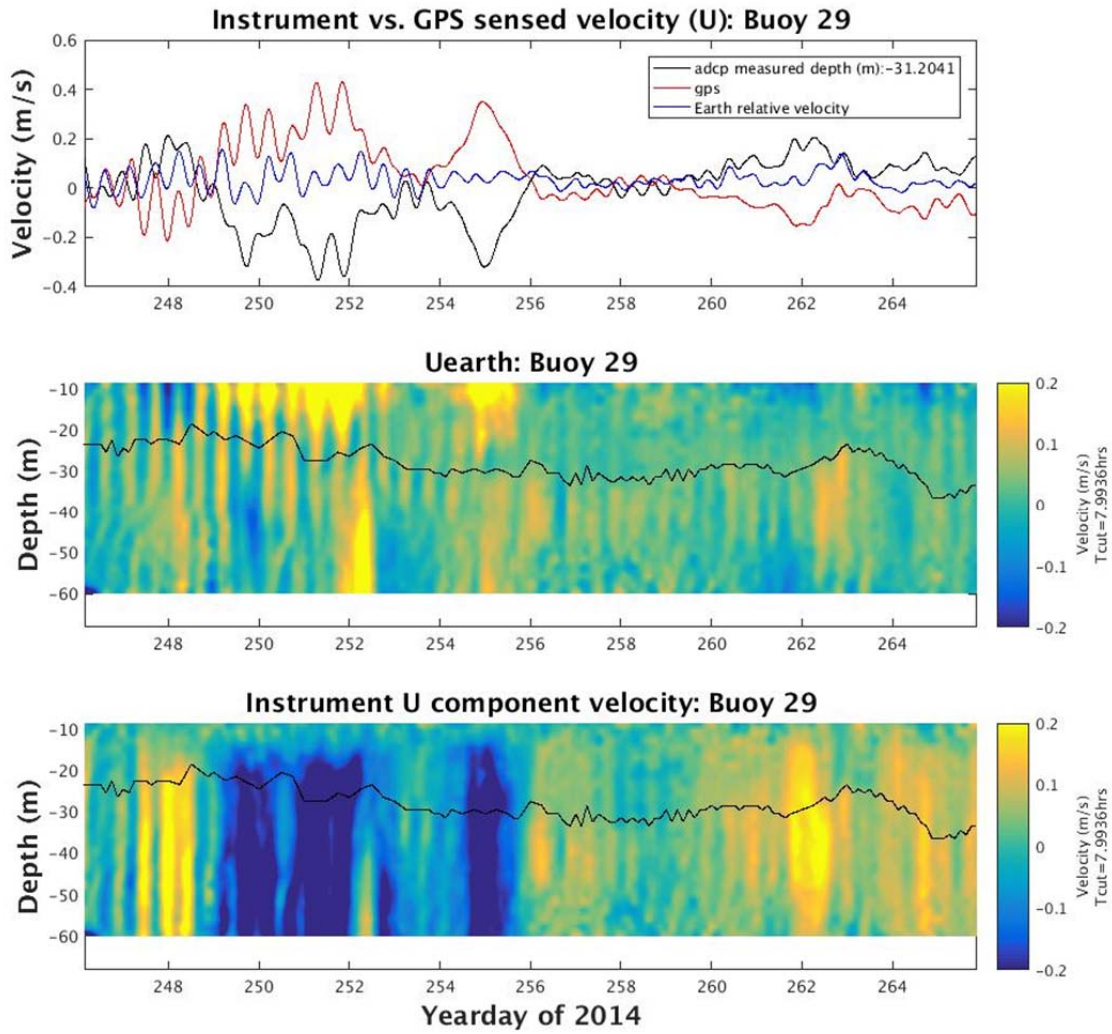
GPS *u* component velocity in red, compared to ADCP measured *u* component velocity at -31.2 m in black. Timeseries is for yeardays 246.5–266. The blue line between the two is the addition of ADCP velocity and GPS velocity, giving the actual Earth relative *u* component current velocity at -31.2 m depth (top panel). Earth relative *u* component velocity profile timeseries (middle panel). ADCP *u* component velocity profile timeseries (bottom panel).

Figure 15. Earth Relative Motion.

ADCP data was interpolated from a 30 min period to the GPS 10 min period. Earth relative current velocity is calculated by adding the GPS velocity to the ADCP velocity, and the summation of the two produces the actual Earth relative current velocity for a particular velocity component (*u* or *v*). The ADCP reads current velocity relative to the ice motion; thus, in a situation with zero actual current, if the AOFB were to be

28

drifting 1 m/s to the East, the ADCP would read a current velocity of -1 m/s (West). Figure 15, top panel, shows the result of this calculation. The u component of GPS data (red line) is added to the corresponding u component of ADCP current velocity (black line). The blue line represents their summation and subsequently the Earth relative current motion at the chosen ADCP depth bin. Figure 15, middle panel shows a profile timeseries resulting from this calculation. The strong 12 hr period striping reveals inertial motion between yeardays 246–253, discussed further in section II.B.7. Figure 15, bottom panel shows the original ADCP referenced u component of velocity. Measurements of shear, N^2, and Richardson number do not require Earth relative velocity components, as these calculations are based upon changes between consecutive depths. However, spectra and inertial calculations require Earth relative components for accurate measurements.

7.   Inertial and Non-inertial Component

Inertial oscillations represent the resonant response to wind forcing with a period at, or just below, the Coriolis period. Internal waves propagating in the pycnocline at this frequency exhibit little vertical amplitude but have strong horizontal velocities. The inertial component of the ADCP velocity profile timeseries were determined through a process of complex demodulation and bandpass filtering. A power spectrum of the Earth relative u component was calculated using the *cpsd* MATLAB function for a 10 day section of the ADCP data (Figure 16). The number of points used to form each Fast Fourier Transform (FFT) was 512 (NFFT), with the number of overlapping samples set as NFFT/2; this offers a balanced tradeoff between time resolution and frequency resolution. Figure 16 shows a plot of the Power Spectral Density (PSD) for yeardays 246.5–256 for three different depths. The black line represents the spectral energy in the middle of the mixed layer with the red line representing the spectral energy at the bottom of the mixed layer, or near the MLD. The shallowest depth of the MLD during the 10 day stretch was -20.1 m, with an average MLD of -25.5 m during the same timeframe. The blue line is the spectral energy at a depth bin always below the MLD.
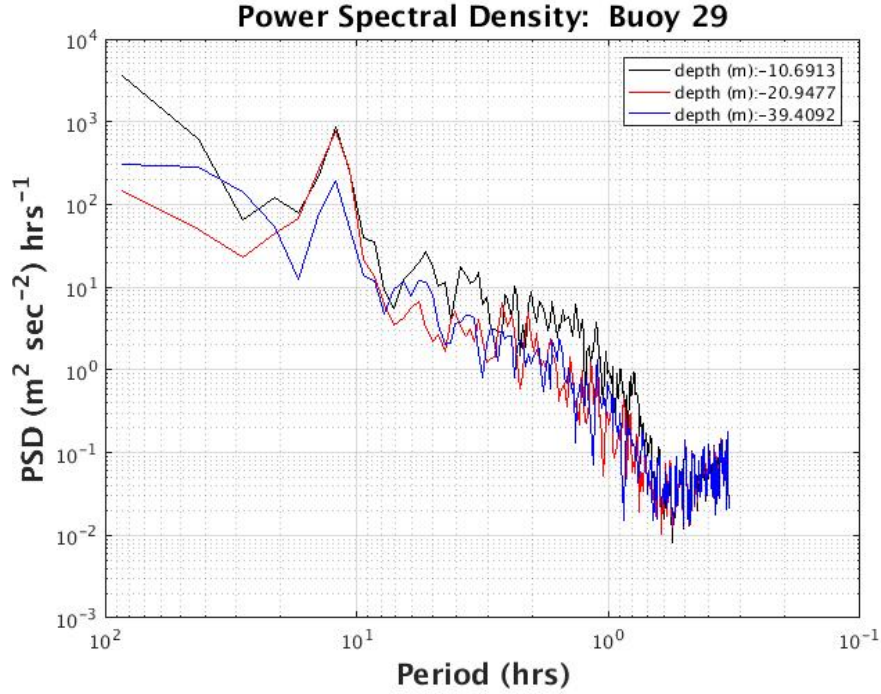
Power Spectral Density (PSD) plot of *u* component Earth relative velocity. Three different depths are used for comparison.

Figure 16. Power Spectral Density

Figure 16 shows nearly an order of magnitude drop in spectral energy when the power spectrum is performed at depth bins below the MLD. This demonstrates the impact the MLD stratification plays in blocking inertial motion coupling into the pycnocline.

The inertial period calculation based upon initial latitude was 12.30 hrs, while the PSD plot shows an inertial peak at 12.150 hrs, within the frequency resolution of the spectrum. The period calculated via latitude was used over the PSD plot. Complex demodulation was used to extract the inertial components of velocity. It first involves high-pass filtering the individual Earth relative velocity components through time. A fourth-order Butterworth filter with a 20-hour period cutoff was used. A complex velocity is formed, then *u* component being multiplied by a cosine wave, and the complex *v* component multiplied by a complex sine wave.

$$\overline{U_i} = (u + iv)e^{i2\pi ft},$$

where f is the Coriolis frequency in Hertz, t is the time vector in seconds, u and v are Earth relative components of current, and Ui is the complex inertial vector. A fourth-order Butterworth low-pass filter with an eight-hour period cutoff acts on the individual inertial components completes the demodulation process that extracts the baseband signal, or our inertial signal. Figure 17 shows the product of complex demodulation and highlights the strong inertial motion occurring between yeardays 246.5–254. The inertial speed is calculated by finding the vector magnitude of u_i and v_i.
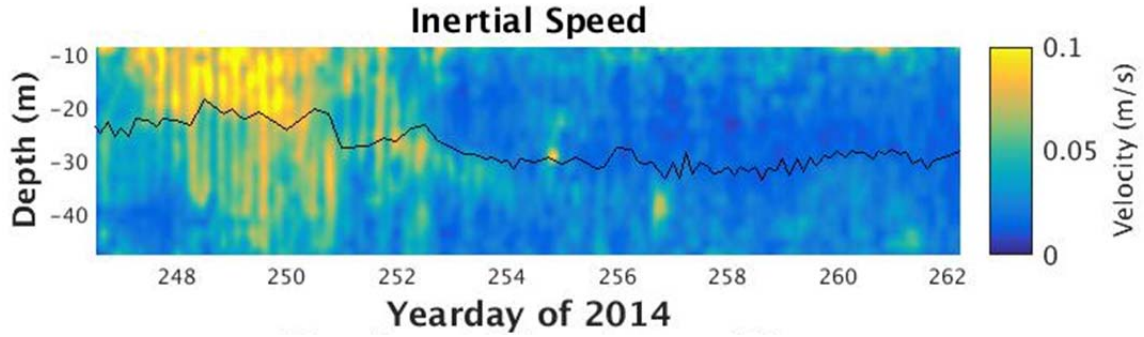
Inertial speed shown as a product of complex demodulation for yeardays 246.5 - 266. Note the strong inertial event at the beginning of the data set.

Figure 17. Inertial and Motion

With the inertial components, u_i and v_i, the inertial component of the gradient Richardson number was calculated. The same process of taking the vertical derivative and using the weighting function to interpolate shear at the mixed layer depth was used (section II.B.4).

8.   **Heat Flux and Heat Content**

Vertical heat flux represents the rate of heat traversing a surface area per unit time with units of Wm^{-2}.

$$HF = \rho c_p < w'T' >$$

where *HF* represents vertical heat flux, *rho* is the density of seawater, and c_p the specific heat capacity of seawater. *w'* and *T'* represent the fluctuating components of the vertical velocity and temperature, respectively.

These turbulence timeseries measurements are made for 40 min and sampled at 2 Hz from by the AOFB flux package. Due to power limitations in sampling and transmitting the full timeseries by Iridium, the 40 min samples are made every 2 hours. Figure 18 shows a 2000 second example of this calculation.
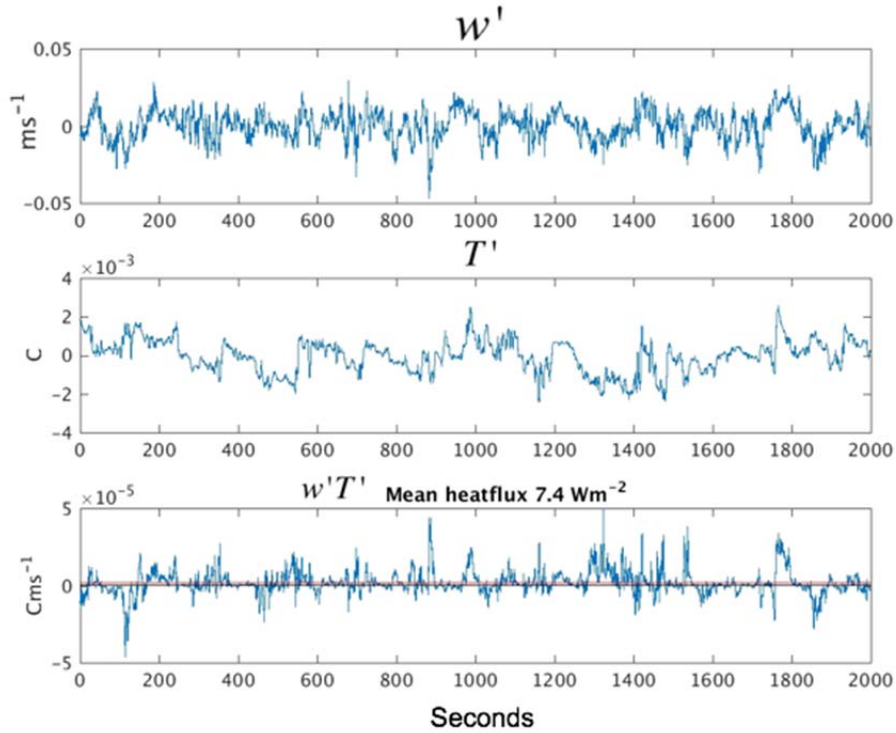

Figure 18. Heat Flux

Figure 18, top panel, represents the turbulent fluctuations in vertical velocity. These fluctuations occur on the order of centimeters per second. The middle panel shows the turbulent fluctuation of temperature that are on the order of a thousands of a degree. When these two turbulent fluctuations are correlated together and ensemble averaged,

then multiplied by the density and specific heat capacity of sea water, the heat flux is obtained in W m^{-2}. The bottom panel demonstrates the highly variable instantaneous correlations between w' and T', while the red line shows the ensemble average of the correlated turbulent fluctuations. This ensemble average is then multiplied by the specific heat capacity and density of seawater to obtain a heat flux of 7.4 W m^{-2} for the 2000 second period.

Pycnocline heat content is calculated by the integration of the difference in temperature between the MLD down to a specified depth, z_e.

$$Hc = \rho c_p \int_{MLD}^{z_e} [T(z) - T(MLD)]dz$$

where ρ is the density of seawater and c_p is the specific heat capacity of seawater. For this study, a 1 m range below the MLD was chosen as z_e. This heat content gives a quantitative estimate of the amount of heat available for entrainment if the potential energy of the stratification over this 1 m depth can be overcome by turbulent, shear-driven entrainment.

THIS PAGE INTENTIONALLY LEFT BLANK

III. RESULTS

## A. DRIFT TRACKS AND TIME PERIODS

AOFB 29 was deployed on 12 August 2014 at 77.431 N, 146.188 W during a 6 day ice camp supported by the Araon ice breaker, and lasted until 05 October 2015 (Figure 19 and 20). ITP 80 was deployed on 11 August 2014 at 77.5101 N, 146.2074 W from the same ice camp and remained operable until 22 May 2015.
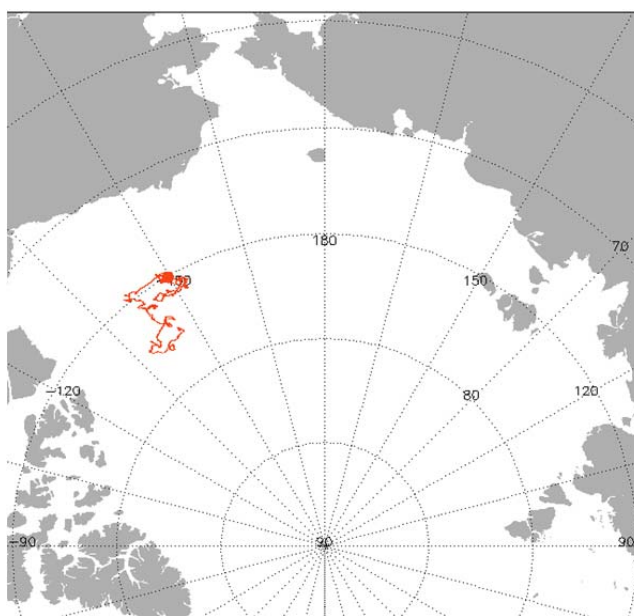
Drift track of ITP 80 and subsequently AOFB 29 which where collocated together in the Beaufort Sea.

Figure 19. ITP Track. Source: IMB 2014.

The drift track of the collocated buoy pair began in the Northwestern Canadian Basin, just east of the Chukchi Plateau (Figure 19 and 20). In response to wind-driven ice drift, the buoy pair meandered east and eventually to the south, crossing the 75N parallel on yearday 343 of 2014. The ice floe then proceeded west towards the Northwind Ridge but was never able to reach the shallowing irregular bathymetry across the Northwind Ridge. The life cycle of the ice floe and corresponding buoys remained over the abyssal features that characterize the Canadian Basin.
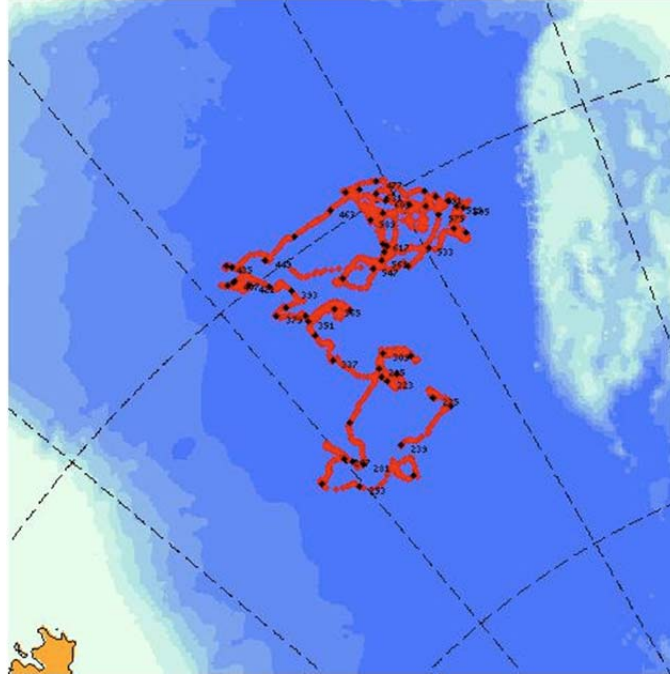
Drift track of AOFB 29. The AOFB remained operable 135 days longer than the ITP.

Figure 20. AOFB track. Source: AOFB 2016.

AOFB current profile data was unavailable during yeardays 228–245 of 2014 and yeardays 243–246 of 2015 due to ADCP setup errors that were remotely corrected. All other sensors were operating during the life cycle of the buoy. However, low acoustic backscatter conditions experienced from yeardays 25–125 of 2015 resulted in noisy current profiles making the data unreliable. The ITP's last day in operation was yearday 143 of 2015. Consequently, parts of this study that utilize ADCP data such as the Richardson number, vertical gradient of shear, and inertial motion are limited to yeardays 246.5 of 2014 to 25 of 2015.

B.   CORRELATION STUDIES

Calculations from ice speed, shear, Richardson number, and MLD amplitude were compared against each other to draw correlations and explore the relationships between the different physical processes. Pearson *r* values and type I error calculations utilized the MATLAB function *corr* when relationship comparisons were plotted. The test to reject

36

the null hypothesis required a type I error of less than 5% ($p < .05$). Yeardays over 365 represent an entrance into the year 2015.

1.   Ice Speed and Shear

Ice speed and shear across the base of the mixed layer were compared from yeardays 246.5–390 in Figure 21. It is hypothesized that increases in ice speed will translate into greater MLD shear, and winter time shear levels should be less than summer time levels due to greater ice concentration and lowered ice mobility. A time series of the two properties reveals the largest ice speeds in the beginning of the study period corresponding to strong fall synoptic systems transiting the site, and the resulting large inertial events that took place at the beginning of our dataset (Figure 21, top panel). Some instances of the coupling between ice speed and MLD shear can be seen between yeardays 255–256 where a large spike in ice speed on yearday 255 translates into a large spike in MLD shear on yearday 256. Another similar example is seen near yeardays 364–365. However, not all instances of increased ice speed are correlated with enhanced MLD shear. Yearday 325 is an example of lower ice speed but average MLD shear. A further look into fall and winter shows no significant drop or increase in MLD shear or ice speed.
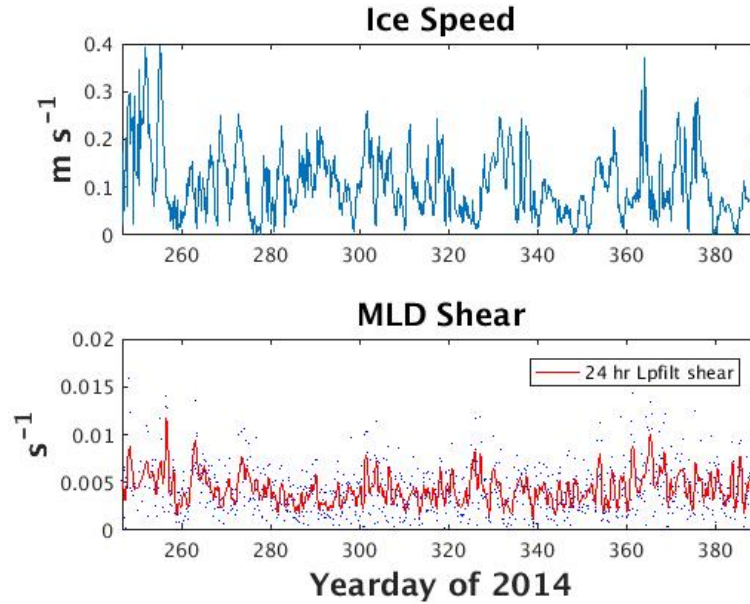
Timeseries of ice speed (top panel) and MLD shear (middle panel) for yeardays 246.5–390. Blue dots in second panel represent raw shear, with 24 hr low pass filtered shear as the red line.

Figure 21. Ice Speed vs. MLD Shear

Ice speed is expected to diminish with increasing ice concentration as the freedom of movement of the ice is decreased. With the reduction in ice speed, a reduction in MLD shear should be seen. The ice acts as a barrier to momentum transfer into the ocean. Surface generated turbulence is only generated when the ice is moving relative to the water. First year ice is often hydraulically smooth underneath; however, multi-year ice is often rough. This basal ice roughness can increase turbulence generation during ice movement and increase MLD shear. AOFB 29 was deployed on a fairly rough multi-year ice floe. Figure 22 shows the correlation between ice speed and MLD shear.
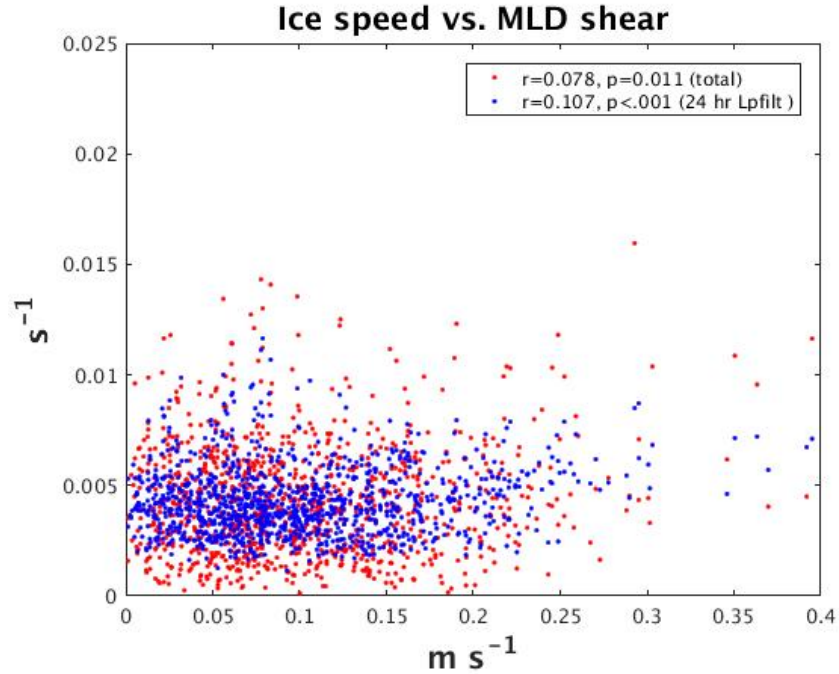
Figure 22. Scatter Plot of Ice Speed vs. MLD Shear

The correlation for raw MLD shear was $r = .078$ ($p = .011$). Using a 24 hr low pass filter on the MLD shear increased correlation and statistical significance slightly ($r = .107, p < .001$). Both raw and filtered shear levels averaged .0043 s^{-1}. The correlations were much weaker than expected when considering the turbulent transfer of momentum from the ice sheet into the ocean mixed layer, bounded by the strong stratification at the MLD.

2. Ice Speed and Richardson Number

The inverse Richardson number was compared to the ice speed for yeardays 246.5–390. It was hypothesized that an increase in ice speed should translate into greater dynamic instability through the increase in vertical shear (Figure 23).
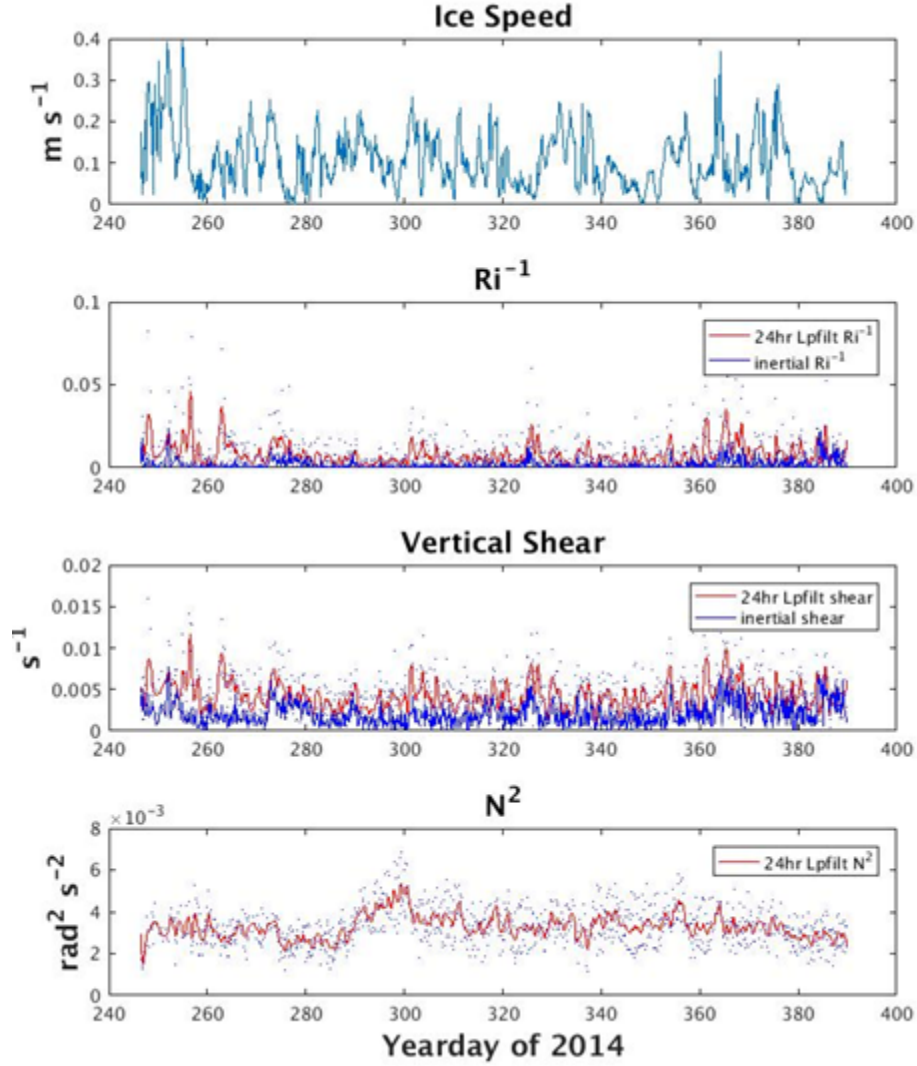
Blue dots represent raw, unfiltered data. Red lines in panels 2–4 represent 24 low pass filtered data. Blue lines in the same panels represent the inertial component of the same parameters. Timeseries is for yeardays 246.5–390.

Figure 23. Comparison of Ice Speed, Richardson Number, Vertical Shear, and N^2

Around yearday 255 a spike in vertical shear results in a spike in inverse Richardson number (Figure 23, middle panel). Later in the timeseries, a small increase in N2 between yeardays 290–300 works to reduce the inverse Richardson number (Figure 23, panel d). The inertial component of the inverse Richardson number sees a short increase near yearday 252, which aligns with the onset of a period of strong inertial activity seen between 246 - 252. However, the increase in seen on yearday 252 is over by yearday 253.

It is surprising how low the inertial shear and inverse Richardson number seen early in the data set are during the strong inertial event seen during this period in Figure 17. Figure 15 shows that substantial inertial energy was still present below the MLD. Lacking a strong vertical difference rather than a lack of inertial energy would create low inertial shear and inverse Richardson numbers. This suggests that the inertial energy from the mixed layer is rapidly coupling into the pycnocline, resulting in low vertical shear values.

Linear regression analysis reveals a poor relationship between the ice speed and inverse Richardson number (Figure 24). The r value was .035 and -.05 for total and inertial correlations, respectively.
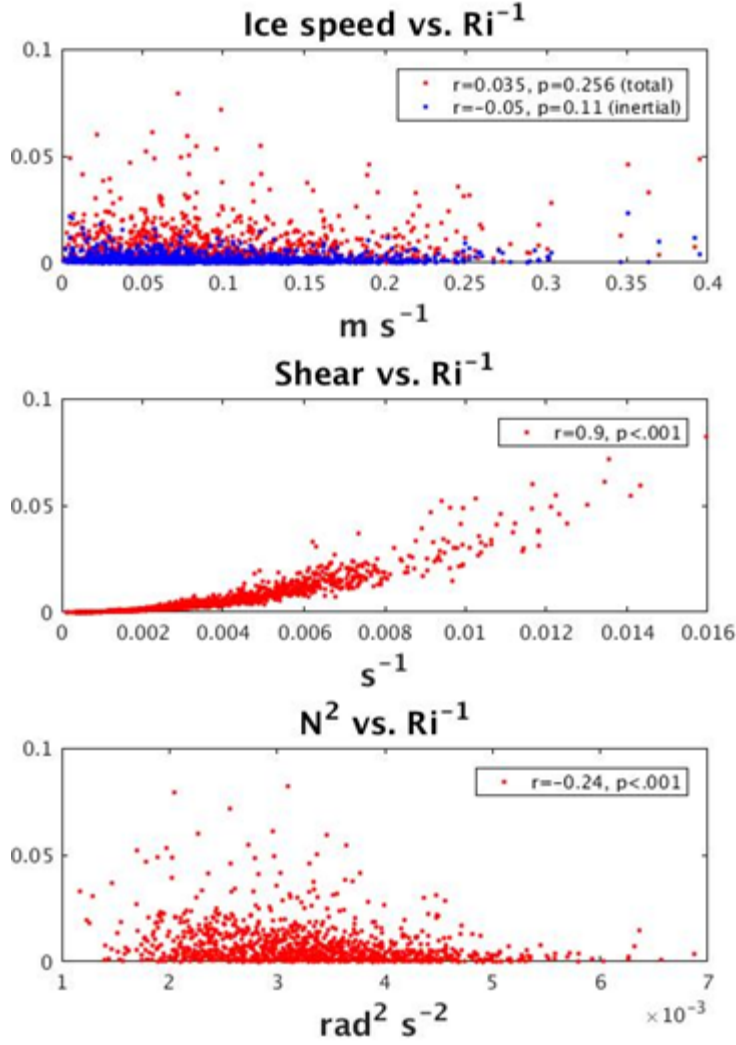
Figure 24. Correlations of Ice Speed, Inverse Richardson Number, Shear, and N^2

A negative correlation for the inertial component is counterintuitive, as it would mean an increase in ice speed would create greater stability in the inertial spectra. However, this thinking is erroneous, as neither relationship was statistically significant ($p > .05$). The correlation between shear and inverse Richardson number was strong at $r = .9$ ($p < .001$) and weak between inverse Richardson number and N^2 ($r = -.24$, $p<.001$), but still significant for the latter. This demonstrates the greater importance shear has in modulating the inverse Richardson number; albeit, it still lacks a statistically significant connection to ice speed.

3. Ice Speed and Heat Flux

It is hypothesized that an increase in ice speed should translate into an increase in heat flux (Figure 25). An erosion of sub-pycnocline heat due to dynamic instability should warm the mixing layer and subsequently create an upward heat flux.
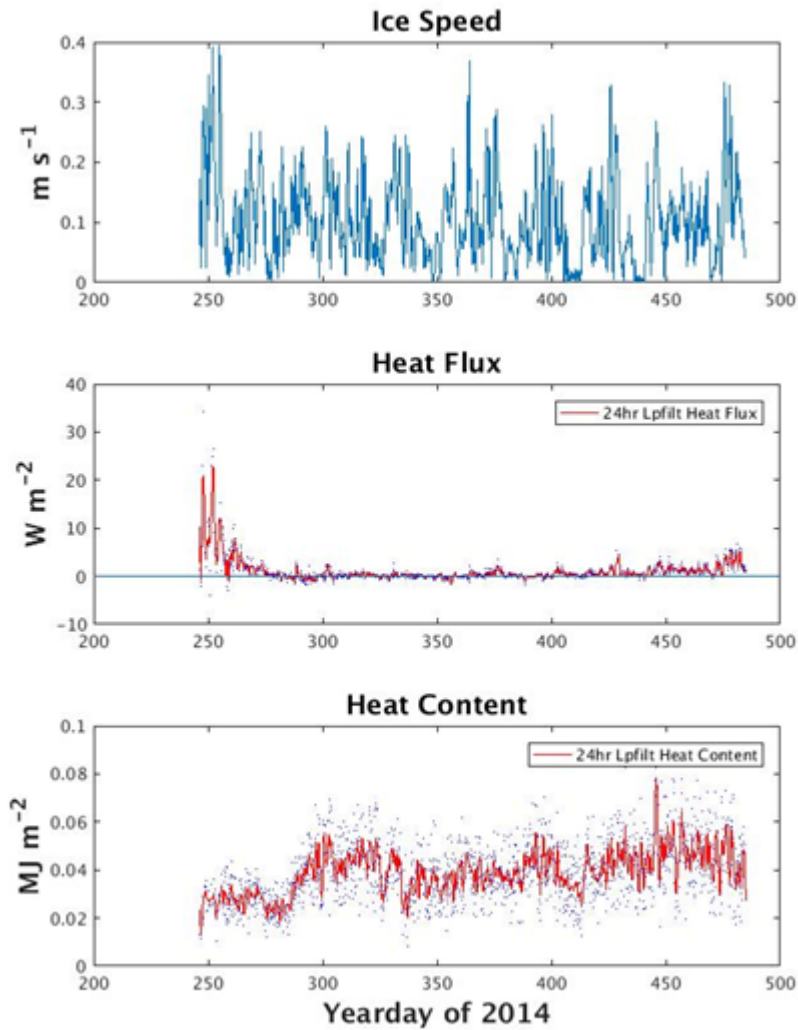
Time series of ice speed, heat flux, and heat content for yeardays 246.5 - 485. Heat content was calculated over 1 m of depth below the MLD.

Figure 25. Time Series of Ice Speed, Heat Flux, and
Heat Content 1 m below MLD.

The most apparent spike in heat flux occurs during the strong inertial activity at the beginning of the data set (Figure 25). The effects of heat flux due to the inertial event fully tapers off by yearday 280, which then heat flux remains mostly positive, between -1 to 4 W m^{-2}. Figure 25 shows that separating the strong inertial event from the rest of the data set reveals a statistically significant relationship between ice speed and heat flux ($r = .569, p<.001$).
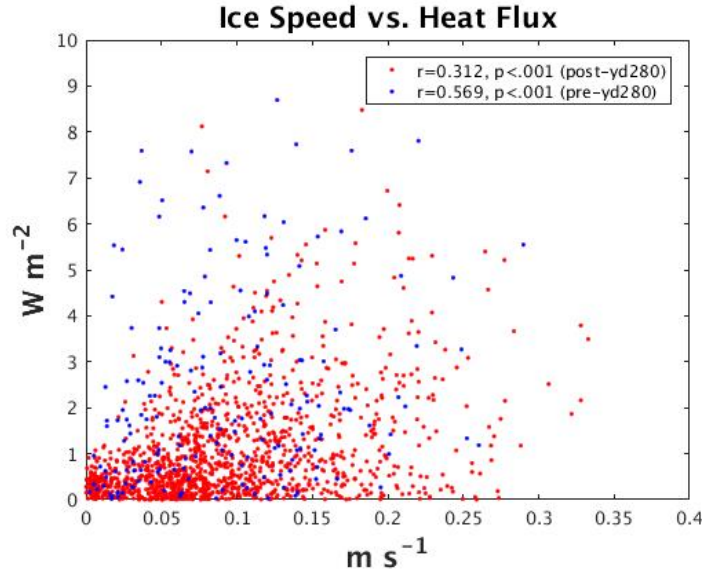
Figure 26. Ice Speed vs. Heat Flux.

Yeardays after 280 still reveal a statistically significant relationship, but a weaker correlation compared to the inertial event ($r = .312, p<.001$) (Figure 26). The inertial event is also when sub-pycnocline heat content is at its lowest, so clearly the dynamic forcing during the strong wind-driven entrainment event dominated the effects of variations in heat trapped just below the mixed layer depth (Figure 27).
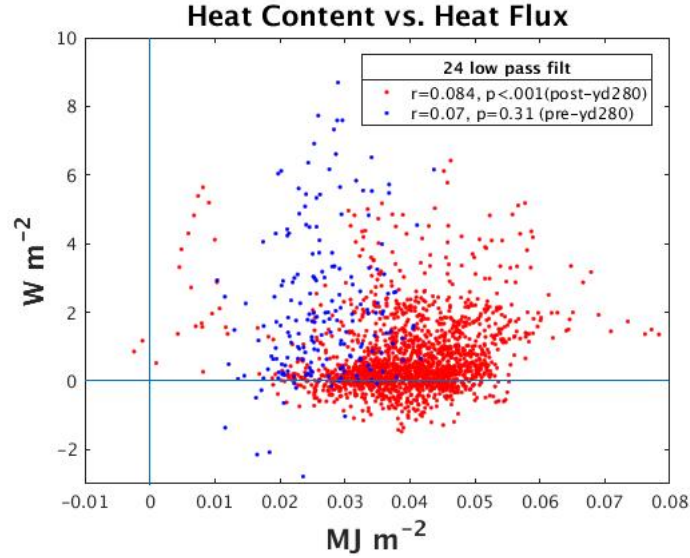
Figure 27. Heat Content vs. Heat Flux

This is further confirmed in a comparison between heat content and heat flux (Figure 27) that reveals weak correlations for pre-yearday 280 (*r=.07, p=.31*) and post-yearday 280 (*r=.084, p<.001*). Although the relationship post-yearday 280 is weak, the relationship is statistically significant. Analyzing the departure from freezing profile timeseries (Figure 28) shows a substantial separation on the order of 15 m between the MLD and warm Pacific water at the start of this interval.
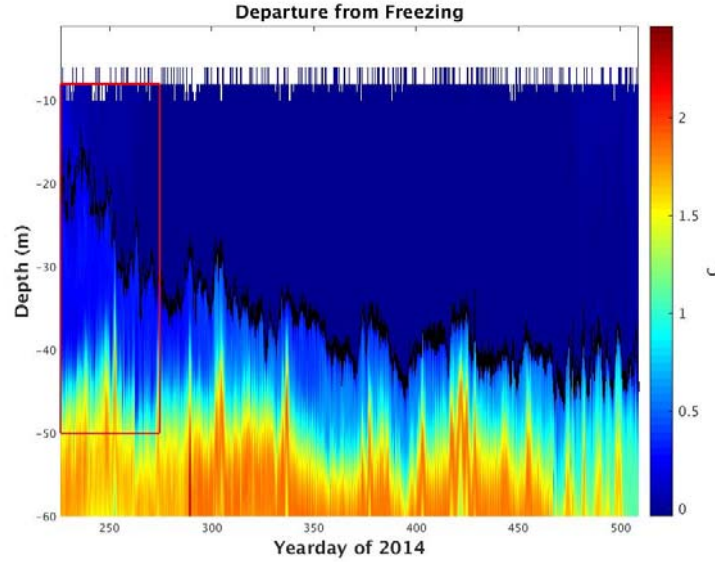
Departure from freezing for yeardays 226 - 508. Black line represents the MLD.

Figure 28. Departure from Freezing

Later in the timeseries, a deepening MLD is seen with an increase in available heat content within the first meter below the MLD. Focusing on near-surface thermal structure between yeardays 226–274 and a depth of -8 m to -50 m reveals significant heat content above our 0.25 Kg m^{-3} definition of MLD (Figure 29). Upper mixed layer heat 0.15 C above freezing can be seen up to yearday 235 in Figure 28. This heat is trapped within the late summer, weak, near-surface stratification seen in Figure 30. This heat is being rapidly entrained during the coincident strong wind event, resulting in the high heat fluxes in Figure 25, middle panel, around yearday 250.

Departure from Freezing
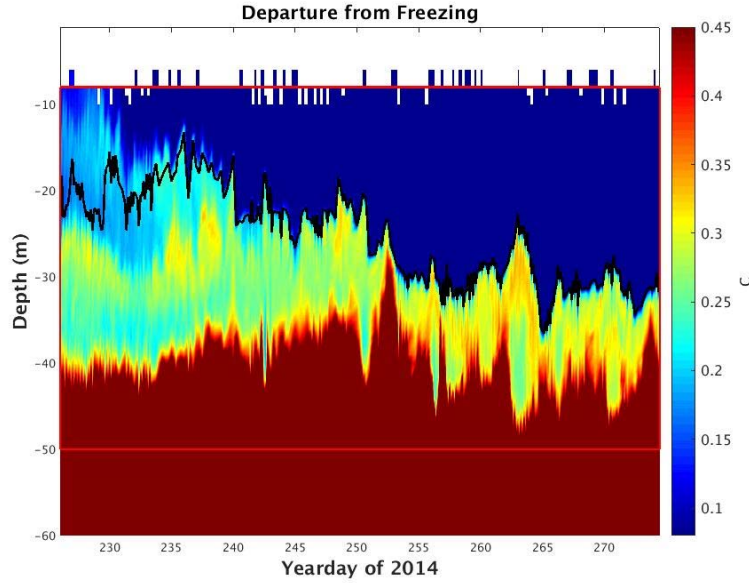
Departure from freezing for yeardays 226 - 275. Black line represents the MLD. Red box
surrounding part of the colored plot is the same red box in Figure 28.

Figure 29. Small Scale Departure from Freezing

The weak stratification seen up to yearday 238 in the upper 20 m of the water
column is formed from strong ice melt during the late summer and represents the late
summer Near Surface Temperature Maximum (NSTM) which is able to block turbulent
mixing further into the water column (Gallaher 2016). During the strong wind driven ice
motion spanning yearday 250, this weak seasonal pycnocline was fully entrained into the
mixed layer and contributed significantly to basal ice melt.

47
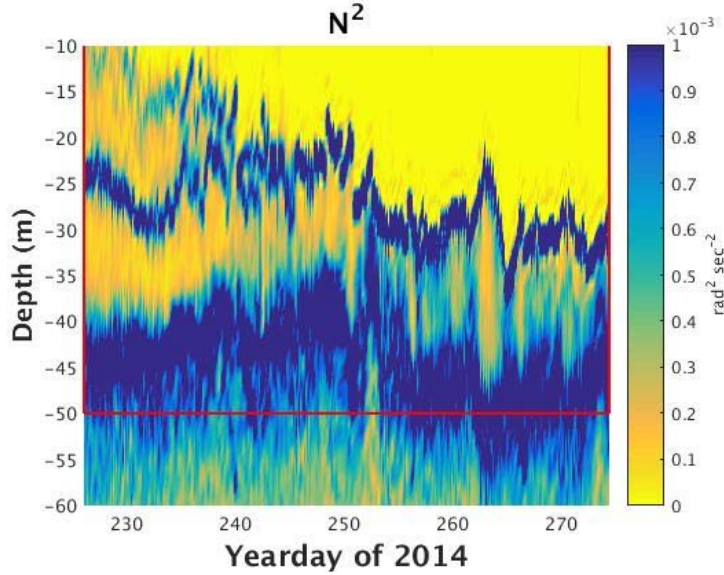
Figure 30. N^2 Stratification profile timeseries for yeardays 225–275.

Figure 30 shows this seasonal pycnocline with a main stratification peak on the order of 4×10^{-4} rad^2 s^{-2} continuing until yearday 240. It is apparent that with each layer of stratification more heat becomes available for entrainment, yet the stratification becomes stronger, making the heat less available for entrainment and diffusion. After yearday 240, the seasonal pycnocline disappears and the .25 kg m^{-3} MLD becomes the first instance of strong stratification in a vertical profile. The low values of stratification of the upper seasonal pycnocline before yearday 240 still play an insulating role in protecting sub-pycnocline heat from entrainment in the mixed layer.

4.   Inverse Richardson Number vs. Heat Flux

It can by hypothesized that an increase in inverse Richardson number should also be followed by an increase in heat flux due to erosion of the pycnocline and entrainment of warmer sub-pycnocline water (Figure 31).
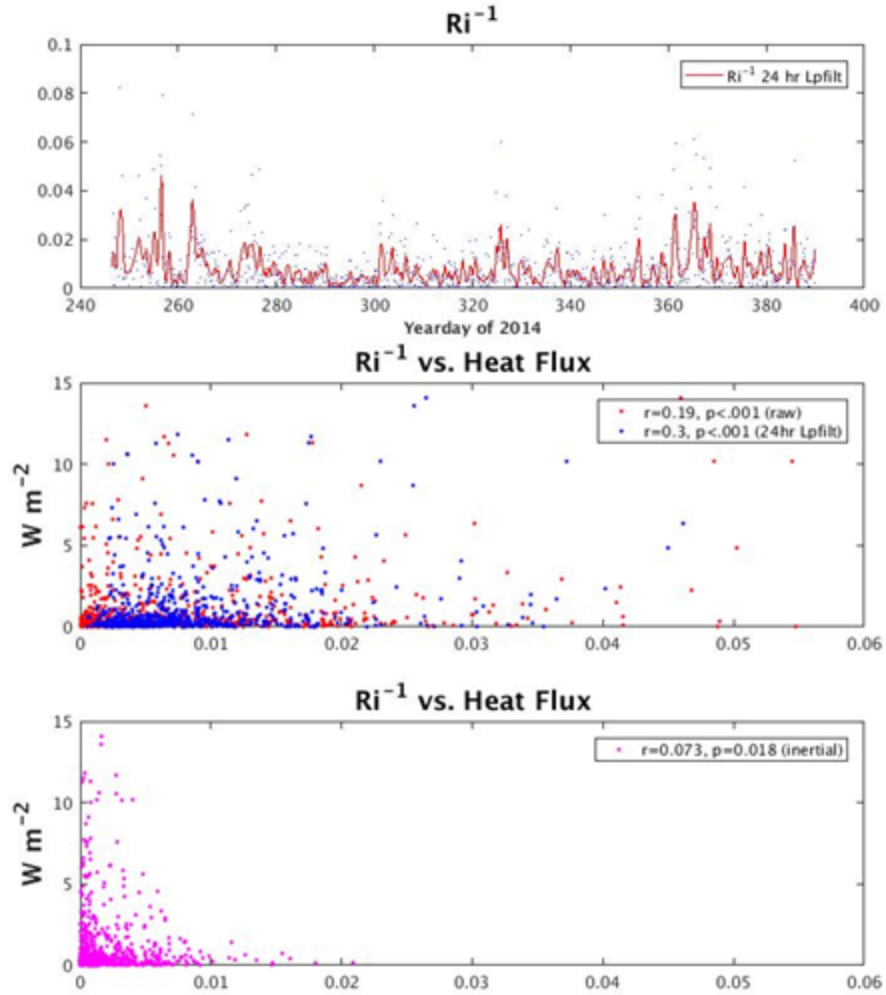
Time series of Inverse Richardson number in panel 1 from yeardays 246.5 - 390. Panel 2 correlates inverse Richardson number against heat flux. Red dots represent raw data, while blue dots represent both inverse Richardson number and heat flux with a 24 hr low pass filter. Third panel represents the much smaller contribution of inertial motion on the inverse Richardson number.

Figure 31. Inverse Richardson Number vs. Heat Flux

Figure 31 shows that when correlating raw heat flux against raw inverse Richardson number, a weak but significant correlation was found ($r = .19, p<.001$). When both heat flux and inverse Richardson number were smoothed with a 24 hr low pass filter, a slightly better correlation was found ($r = .3, p<.001$). The inertial shear only inverse Richardson number saw the weakest correlation with $r = .073$ and type I error at $p = .018$.

THIS PAGE INTENTIONALLY LEFT BLANK

IV. CONCLUSIONS

A. SUMMARY

There was a surprising lack of correlation between ice speed and MLD shear. The two physical mechanisms are naturally concomitant to one another. However, there is not always a one-to-one relationship. As the ice accelerates, it transfers momentum to the underlying ocean. This momentum transfer of the sea ice to the underlying ocean is greater with the presence of multi-year ice with rafting and ridging elements creating a hydro-dynamically rough surface. The time lags associated with acceleration of the fluid and formation of a sheared mixing layer that reaches the MLD reduces direct correlation with ice speed. The deeper the MLD, the greater the turbulent energy that is required to reach its depth and allow corresponding shear and entrainment. The MLD depth is dependent on seasonal variations and lateral gradients in the ocean as the buoy drifts over the relatively stationary ocean. On short time scales, mesoscale eddies can also affect MLD depths, which in turn would affect the magnitude of shear.

Baroclinic instability and internal wave breaking can generate shear across the MLD that may not be predicated by ice speed. As Timmermans et al. (2012) demonstrated, measuring the effects of baroclinic instability and restratification requires spatial observations rather than single point measurements. A shallow stratification created through baroclinic instability can be can be eroded if turbulence is strong enough. However, it dampens energy that may reach the .25 kg m^{-3} MLD. Even weak shallow stratification just below the ice dampens turbulence and momentum transfer down through the water column. Figures 25, middle panel, and Figure 29 demonstrate that considerable heat is available for basal ice melt during powerful mixing and shallow entrainment events.

The effect of defining the MLD can be a challenge when multiple layers of stratification are present, and one criteria for its definition may not fit all moments in the timeseries. Defining the MLD through a .01 kg m^{-3} bulk potential density difference would better characterize the seasonal pycnocline early in the data set compared to the

.25 kg m^{-3} criteria. However, in between mixing events and lateral restratification the .01 kg m^{-3} results in erratic depths. This results in erratic values for shear, inverse Richardson number, and heat content below the .01 kg m^{-3} MLD. The .25 kg m^{-3} criteria worked well during the majority of the available time series.

Measurements of shear are highly dependent upon ADCP performance, noise, and available scatterers in the water column. The data was ameliorated by limiting processing to high backscatter days, interpolating across low acoustic Doppler correlation data, and using low pass filtering. Correlations between ice speed and inverse Richardson number were not statistically significant; however, due to the low variation in stratification of the MLD, the inverse Richardson number was largely modulated by the available shear. A low correlation of MLD shear would also give a predilection towards a lower correlated inverse Richardson number.

The relationship between ice speed and heat flux had the highest correlation values. The strong inertial event and resulting heat flux event was processed separately from the rest of the data to study the role of inertial energy in the system. In both the inertial event and post inertial event cases, ice speed and heat flux were moderately correlated with each other, and statistically significant. This is as expected within the theoretical framework of dynamic instability. This illustrates that strong inertial events can potentially capture large amounts of heat that become immediately available for basal ice melt. Inertial events are dampened when internal ice stresses are high (McPhee 2008). It can be theorized that continuing lower concentrations of sea ice nominally seen during the late summer acted to magnify inertial motions and corresponding vertical heat flux. However, the main reason for the initial high heat fluxes were revealed in the high resolution view of the ocean mixed layer temperature and stratification. This shallow, weakly stratified heat was readily mixed out during the strong wind and ice motion event.

The amount of vertical heat flux may not be directly associated with the sub-pycnocline heat content in the 1 m below MLD as the comparisons show. Although the correlation between heat content and heat flux was statistically significant, the correlations were weak ($r < .1$). This somewhat arbitrary measure of heat content showed very little variation during this 238 day sample of the Canadian Basin. Analysis of the

temperature structure immediately below the MLD showed warmer water, and enhanced stratification, but not at the level of heat content contained within the Pacific layer (Figure 29). Consequently, the pycnocline diffusivity is likely to be strongly limiting heat flux up to the MLD where the heat becomes available for entrainment.

The inverse Richardson number was at its highest correlation with the heat flux when the data was smoothed with a 24 hr low pass filter. The inverse Richardson number was highly modulated by the MLD shear rather than N^2 during this time series. With a correlation of $r = .3$, it was below what was expected. However, measuring the MLD shear is dependent upon the criteria for defining the MLD and what bulk density difference was used. Correlating the inverse Richardson number with the heat flux also assumes that no NSTM is present in the timeseries. Although a NSTM was present early in our timeseries, it was gone before inverse Richardson number calculations began. The strength of the MLD stratification may have lowered correlation between inverse Richardson number and heat flux since stronger stratification allows greater fluctuations in shear before dynamic instability takes place, and subsequent heat flux rises above molecule diffusivity levels.

B.   FURTHER STUDIES

An area of interest for future research would be a better estimate of heat flux to heat content, and the ability to determine the exact depth of entrainment that took place. With an exact depth of entrainment, the true heat content available to the mixed layer can be calculated. Another interesting area of interest is in the correlation between ice speed and heat flux. Although the correlations in this study were moderately low ($.3 < r < .5$), the inclusion of more AOFB and ITP buoys could help to sharpen this relationship. From a remote sensing aspect, the ability to have a prediction of heat flux values simply based on ice speed is a powerful consideration in the way forward, but will be limited by regional variations in upper pycnocline heat content. This study was fortunate to work in the Canadian Basin, as regions with irregular bathymetry may prove to be more challenging in this regard. Regions with high internal wave breaking and tidal

interactions along with upwelling zones may add more variables to an already complicated effort.

This thesis demonstrates that the Arctic is a complex and dynamical system with physical relationships that are clearly multi-variate and interconnected. The Arctic is also a delicate ecosystem and its future is uncertain at the current level of global warming and sea ice decline. There is still much to learn about this cold, harsh environment, and it is of hope that this thesis contributes to that knowledge.

LIST OF REFERENCES

Aagaard, K., L. K. Coachman, and E. Carmack, 1981: On the Halocline of the Arctic Ocean. *Deep-Sea Res.,* **28**, 529–545.

Aagaard, K., 1981: On the deep circulation in the Arctic Ocean. *Deep-Sea Res.*, **28A**, 251–268.

AOFB, 2016: Autonomous Ocean Flux Buoy (AOFB) program. Accessed 16 October, 2016. [Available online at http://www.oc.nps.edu/~stanton/fluxbuoy/index.html.]

D'Asaro, E. A., P. Van Meurs, and P. P. Niiler, 1995: Upper-ocean inertial currents forced by a strong storm. Part I: Data and comparisons with linear theory. *J. Phys. Oceanogr.*, **25**, 2909–2936.

Gallaher, S. G., T. P. Stanton, W. J. Cole, S. T. Toole, J. M. Wilkinson, T. Maksym, and B. Hwang, 2016: Evolution of a Canada Basin ice-ocean boundary layer and mixed layer across a developing thermodynamically forced marginal ice zone. *J. Geophys. Res., 121, 6223–6250.*

Garrett, C., and W. Munk, 1972: Space-time scales of internal waves. *Geophys. Fluid Dyn.,* **2**, 255–264.

Gill, A. E., 1982: *Atmosphere-Ocean Dynamics*. Academic Press, 662 pp.

Halle, C., and R. Pinkel, 2003: Internal wave variability in the Beaufort Sea during the winter of 1993/1994. *J. Geophys. Res.*, **108**, 3210, doi:10.1029/2000JC000703.

IMB, 2014: Ice Mass Balance Buoys. Accessed 16 October, 2016. [Available online at http://imb.erdc.dren.mil/2014F.htm.]

IPCC, 2014: *Climate Change 2014: Synthesis Report. Contribution of Working Groups I, II and III to the Fifth Assessment Report of the Intergovernmental Panel on Climate Change*. IPCC, Geneva, Switzerland, 151 pp.

Krishfield, R., J. Toole, J. Proshutinsky, and M. L. Timmermans, 2008: Automated ice-tethered profilers for seawater observations under pack ice in all seasons. *J. Atmos. Oceanic Technol.*, **25**, 2091–2105.

Levine, C., A. Paulson, and J. H. Morison, 1985: Internal waves in the Arctic Ocean: Comparison with lower latitude observations. *J. Phys. Oceanogr.*, **15**, 800–809.

Maykut, G. A., 1978: Energy exchange over young sea ice in the central Arctic. *J. Geophys. Res.*, **87**, 7971–7984.

McPhee, M., 2008: *Air-Ice-Ocean Interaction: Turbulent Ocean Boundary Layer Exchange Process.* Springer Science and Business Media, 216 pp.

Osborn, T. R., and C. S. Cox, 1972: Oceanic fine structure. *Geophys. Fluid Dyn.,* 3, 321–345.

Perovich, D. K., J. A. Richter-Menge, K. F. Jones, and B. Light, 2008: Sunlight, water, and ice: Extreme Arctic sea ice melt during the summer of 2007. *Geophys. Res. Lett.*, **35**, doi:10.1029/2008GL034007.

Pinkel, R., 2008: The wavenumber-frequency spectrum of vortical and internal-wave shear in the western Arctic ocean. *J. Phys. Oceanogr.*, **38**, 277–290.

Pond, S., and G. L. Pickard, 1978: *Introductory Dynamic Oceanography*. Pergamon Press, 258 pp.

Price, J. F., R. A. Weller, and R. Pinkel, 1986: Diurnal cycling: Observations and models of the upper ocean response to diurnal heating, cooling, and wind mixing. *J. Geophys. Res.—Oceans*., **91**, 8411–8427.

Randall, D., J. Curry, D. Battisti, G. Flato, R. Grumbine, S. Hakkinen, D. Martinson, R. Preller, J. Walsh, and J. Weatherly, 1998: Status of and outlook for large-scale modeling of atmosphere-ice-ocean interactions in the Arctic. *Bull Amer. Meteor. Soc.*, **79**, 197–219.

Serreze, M. C., and R. G. Barry, 2005: *The Arctic Climate System*. Cambridge University Press, 415 pp.

Shaw, W. J., and T. P. Stanton, 2014: Vertical diffusivity of the Western Arctic Ocean halocline. *J. Geophys. Res.-Oceans*., **119**(8), 5017–5038.

Shaw, W. J., T. P. Stanton, M. G. McPhee, J. H. Morison, and D. G. Martinson, 2009: Role of the upper ocean in the energy budget of Arctic sea ice during SHEBA. *J. Geophys. Res.-Oceans*., **114**, doi:10.1029/2008JC004991.

Simmonds, I., 2015: Comparing and contrasting the behavior of Arctic and Antarctic Sea ice over the 35-year period 1979–2013. *Ann. Glaciol*., **56**, 18–28.

Smith, W. O., and J. M. Grebmeier, 1995. *Arctic Oceanography: Marginal Ice Zones and Continental Shelves*. Springer-Verlag, 288 pp.

Timmermans, M. L., S. Cole, and J. Toole, 2012: Horizontal density structure and restratification of the Arctic ocean surface layer. *J. Phys. Oceanogr.*, **42**, 659–668.

Toole, J. M., M. L. Timmermans, D. K. Perovich, R. A. Krishfield, A. Proshutinsky, and J. A. Richter-Menge, 2010: Influences of the ocean surface mixed layer and thermohaline stratification on Arctic sea ice in the central Canada Basin. *J. Geophys. Res.*, **115**, doi:10.1029/2009JC005660.

Tsamados, M., D. Feltham, D. Schroeder, S. Farrel, N. Kurtz, and S. Laxon, (n.d.): Variable atmospheric and oceanic drag over Arctic sea ice. Accessed 11 October 2016. [Available online at http://www.whoi.edu/ fileserver.do?id=169297&pt=2&p=180851.]

Wadhams, P., 2012: Arctic ice cover, ice thickness and tipping points. *R. Swedish Acad. Sci.*, **41**, 23–33.

THIS PAGE INTENTIONALLY LEFT BLANK

INITIAL DISTRIBUTION LIST

1.   Defense Technical Information Center
        Ft. Belvoir, Virginia

2.   Dudley Knox Library
        Naval Postgraduate School
        Monterey, California